Chemical Engineering Journal 529 (2026) 172848

Contents lists available at ScienceDirect

Chemical Engineering Journal

journal homepage: www.elsevier.com/locate/cej

Kinetic modeling and parameter estimation of thin-layer iron oxide reduction with hydrogen in a fixed-bed reactor

Emiliano Salucci [a,b,*], Antonio D'Angelo [a,b], Vincenzo Russo [b], Henrik Grénman [a], Henrik Saxén [a]

[a] Åbo Akademi University, Henrikinkatu 2, Turku, 20500, Finland
[b] University of Naples Federico II, Via Cintia 26, Napoli, 80126, Italy

ARTICLE INFO

Keywords:
Hydrogen
Direct reduced iron
Green ironmaking
TCD
SCM
Kinetic modeling

ABSTRACT

In recent years, the reduction of iron ores by hydrogen has gained increased attention, as it could significantly reduce greenhouse gas emissions from the metallurgical sector in the near future. In order to enable a rapid technological development in this direction, it is essential to start from the fundamentals of the reduction process, i.e., to investigate the intrinsic kinetics of iron oxide reduction. In this work, an in-depth kinetic investigation of the reduction of pure powdered iron oxides in a packed bed reactor-like system was carried out. The conversion of the solid reactant was followed by measuring the outlet gas composition with the help of rapidly responsive thermal conductivity, and the kinetics of the reduction were mathematically modeled. Based on the assumptions behind the shrinking core model, a mathematical model was developed for a thin fixed-bed reactor that successfully described the experimental data by accurately determining key kinetic parameters. The results show that the different reaction steps are chemically controlled, except for the first step, which is governed by a mixture of internal diffusion and chemical control.

1. Introduction

Although iron and steel have been produced for many centuries, several technical innovations in the second half of the 18th century laid the foundations for future mass production. In particular, the introduction of coke in the blast furnace (BF) proved to be decisive, as it served as a cost-effective source of heat and reducing agents [1]. Through continuous technical development, the steel industry was able to significantly increase its efficiency and has reached an annual production of almost 2000 million tons of steel, of which today 73.7% is produced in the blast furnace–basic oxygen furnace (BF-BOF) process [2]. This sector is currently the largest industrial consumer of coal, accounting for approximately 15% of global consumption [3]. Unsurprisingly, the reliance on carbon-based technologies leads to significant carbon dioxide (CO_2) emissions, estimated at around 2.6 Gt/year [4]. This makes the steel industry one of the largest contributors to greenhouse gas emissions and is responsible for around 8% of direct global industrial CO_2 emissions [2]. Across the entire complex production chain, 70% of the CO_2 emissions come from the blast furnace process, mainly due to the need for high operating temperatures and the reduction of iron ores (iron oxides) [5]. The heart of the process, part of what is known as primary steelmaking, begins with an initial pretreatment and agglomeration of the powder raw materials (coking and sintering/pelletizing), followed by the alternating charging of coke and the preprocessed ore into the blast furnace. At the same time, hot air enriched with oxygen (hot blast) and pulverized coal are injected through nozzles ("tuyeres") in the lower part of the furnace [6]. The interaction between the oxygen in the blast and the coke and injected hydrocarbons leads to a partial combustion of the carbon, which not only provides energy for the operation of the furnace but also enables the formation of carbon monoxide (CO). This, in turn, enables the conversion of oxides into metallic iron through a series of chemical reactions, generally starting from hematite (Fe_2O_3), and all leading to the formation of carbon dioxide [7]:

$$3Fe_2O_{3(s)} + CO_{(g)} \rightleftharpoons 2Fe_3O_{4(s)} + CO_{2(g)} \qquad \Delta H_r^{800^\circ C} = -7\,\mathrm{kJ/mol}$$

$$Fe_3O_{4(s)} + CO_{(g)} \rightleftharpoons 3FeO_{(s)} + CO_{2(g)} \qquad \Delta H_r^{800^\circ C} = +6\,\mathrm{kJ/mol}$$

$$FeO_{(s)} + CO_{(g)} \rightleftharpoons Fe_{(s)} + CO_{2(g)} \qquad \Delta H_r^{800^\circ C} = -18\,\mathrm{kJ/mol}$$

As shown, the reversible reaction network includes two intermediate species: magnetite (Fe_3O_4) and wüstite (FeO), and the energy

* Corresponding author at: Åbo Akademi University, Henrikinkatu 2, Turku, 20500, Finland.
E-mail address: emiliano.salucci@abo.fi (E. Salucci).

https://doi.org/10.1016/j.cej.2026.172848
Received 4 August 2025; Received in revised form 18 December 2025; Accepted 9 January 2026
Available online 17 January 2026

contribution of these reactions is clearly exothermic [8]. In addition to the reactions listed above, also the reverse Boudouard reaction [9]

$$2CO_{(g)} \rightleftharpoons C_{(s)} + CO_{2(g)} \qquad \Delta H_r^{800^\circ C} = -85\,\mathrm{kJ/mol}$$

occurs at higher temperatures, developing CO_2 and C in the presence of CO. In the upper furnace, the reverse Boudouard reaction may occur, leading to deposition of carbon (e.g., on iron [9]). The high temperatures in the blast furnace, which can exceed 2000 °C in the lower zones, favor two critical conditions for the process: improved kinetics of oxygen removal from the iron oxides and melting of the metal. In the lowest part of the furnace, i.e., the hearth, molten slag containing inorganic compounds such as silicates and aluminosilicates are separated from the molten metal due to their different densities. The role of coke is essential for three additional reasons: it maintains the gas permeability of the BF by providing coke slits in the cohesive zone (where the iron ores start to soften and finally melt) through which the gas can flow, and permeability for the gas and liquids in the lower zone [10]. The coke also supports the bed as the tiny solid species in the lower furnace, and finally ensures a sufficient carbon content in the hot metal (around 4%) in the melt, which is a prerequisite in the downstream BOF process where the carbon dissolved in the hot metal is oxidized, heating the melt as it is decarburized to obtain an alloy with desired mechanical properties [11].

This overview makes it clear that carbon is an inherent component in current ironmaking technologies, which need to be fundamentally revised as the CO_2 emissions should be substantially decreased. In particular, a chemical alternative to CO and lower operating temperatures are required. Alternative processes such as the Midrex were already proposed in the 1960s [12], utilizing natural gas as the source of energy and reductants. They are referred to as direct reduction (DR) and are based on solid-gas reactions between iron ores and a reducing agent, which is a mixture of CO and hydrogen (H_2), generally obtained by methane reforming. The reaction network is thus extended to include the following reduction reactions, which are stoichiometrically similar to those already listed:

$$3Fe_2O_{3(s)} + H_{2(g)} \rightleftharpoons 2Fe_3O_{4(s)} + H_2O_{(g)} \qquad \Delta H_r^{800^\circ C} = -1\,\mathrm{kJ/mol}$$

$$Fe_3O_{4(s)} + H_{2(g)} \rightleftharpoons 3FeO_{(s)} + H_2O_{(g)} \qquad \Delta H_r^{800^\circ C} = +17\,\mathrm{kJ/mol}$$

$$FeO_{(s)} + H_{2(g)} \rightleftharpoons Fe_{(s)} + H_2O_{(g)} \qquad \Delta H_r^{800^\circ C} = +16\,\mathrm{kJ/mol}$$

As the chemical nature of the reactions suggests, H_2 reduction, unlike CO reduction, is generally endothermic [8]. This requires careful evaluation of the energy balance of the DR furnace to maintain optimal operating temperatures. However, these processes do not require the extreme temperatures of the BF–BOF route as no molten iron is produced at this stage. The reduced iron ore or pellets, usually referred to as direct reduced iron (DRI), are later melted in an electric arc furnace [13]. From a thermodynamic perspective, the reactions of iron oxides with CO or H_2 have been extensively studied and can be summarized in the Baur–Glässner/Chaudron diagram in Fig. 1 [8].

The diagram presents the stability regions of solid iron oxides and iron as a function of the Gas Oxidation Degree (GOD) and temperature. The GOD is the ratio between the concentration of the oxidizing species (CO_2 or H_2O) and the total concentration of the oxidizing and reducing species. In the absence of inert gasses, the GOD corresponds to the molar fraction of the oxidizing agent. The diagram indicates the existence of an eutectoid point above 570 °C at which FeO is formed. In the diagram, GOD = 1 corresponds to no reduction potential of the gas. For Fe_2O_3, for example, a gas with GOD <1 can reduce it at any temperature, i.e., even in the presence of infinitesimal amounts of reducing agent. In the other stability ranges, there are significant differences between CO and H_2. Due to the different monotonic trends of the FeO–Fe equilibrium curves, H_2 reduction above 800 °C becomes advantageous as the stability field of iron expands, while it contracts for CO-based reduction.

To reduce the carbon footprint of the steel industry, the most promising alternative today is to use green hydrogen instead of CO in the reduction steps [14]. A key factor to be explored is therefore the redox kinetics and morphological evolution of the solid material in the presence of H_2. The scientific literature is very extensive in terms of practical and methodological aspects [15]. The most commonly used setup for reduction experiments is a thermogravimetric system [16,17], which evaluates the conversion of iron oxides to metallic iron based on the weight loss of the solid sample. An alternative is the indirect evaluation of solid metallization of the sample via the analysis of the gas composition at the outlet, using balance equations to follow the oxygen transferred from the solid to the gas phase [18,19]. Among the operating parameters, temperature plays a pivotal role due to its wide-ranging influence on kinetics [20,21], thermodynamics [22,23] (Fig. 1), fluid dynamics [24,25] and morphological changes [26,27]. Another key factor is the nature of the solid and its intrinsic properties, such as porosity [28,29] and shape [30,31]. The literature covers reduction experiments of both pure [32,33] and commercial materials [34,35] and shows considerable differences in the transient morphological evolution [36,37] especially in the case of pellet reduction where tortuosity and porosity changes can influence crucially the gas diffusion [38,39]. Furthermore, the effect of gangue remains unclear in many respects, even though various studies have attempted to identify its influence through rigorous experimental or numerical approaches [40,41]. Granulometric distribution is also of critical importance, with particle sizes ranging from nano powders [42] through grains or fines [43] to commercial pellets up to tens of millimeters in diameter [44]. For the gas used in the experiments, it is essential to properly consider the solid behavior in order to avoid limiting phenomena such as gas starvation and external diffusion. Therefore, many studies focus on variations in composition [45,46] and linear gas velocity (i.e., volumetric flow rate) [47,48]. From a modeling perspective, Avrami models are often used in studies of heterogeneous reactive processes to simplify nucleation and growth dynamics [49,50]. More comprehensive models include the Shrinking Core Model (SCM) [51,52], the grain model (GM) [53,54] or the random pore model (RPM) [55,56]. At pilot plant or furnace scale, Computational Fluid Dynamics (CFD) models enable detailed fluid dynamic analysis and the exploration of theoretical alternatives to conventional processes that could drive future industrial development [57,58].

From this broad spectrum of experimental and modeling approaches, kinetic parameters of surprising discrepancy have been reported. For example, various authors have reported activation energies between 18 and 246 kJ mol^{-1} [59], with standard deviations often reaching 80% of the average value [60]. This leads to very different conclusions about the

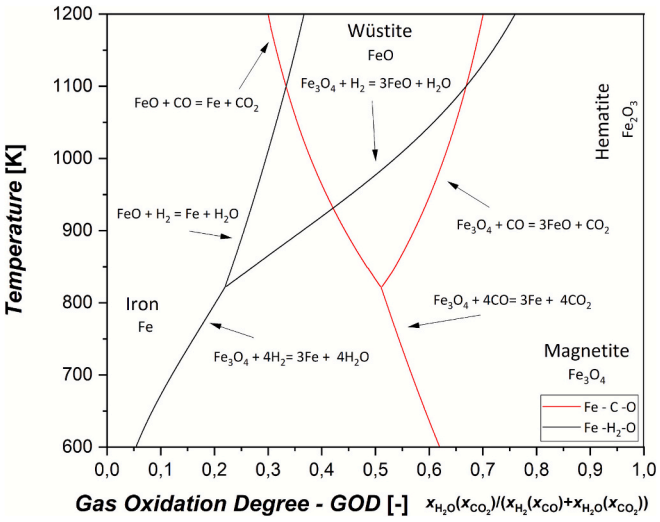

Fig. 1. Baur–Glässner/Chaudron thermodynamic diagram [8].

rate-limiting steps of the reduction process, which may be kinetic [61], diffusive [62] or shifting regimes [63]. Such inconsistencies highlight a critical gap in current kinetic modeling: the lack of systematic approaches to isolate intrinsic chemical kinetics from transport and morphological effects. To address this, the present study introduces a combined experimental and modeling framework designed to minimize these interferences and provide reliable kinetic parameters for hydrogen-based iron oxide reduction. By accurately evaluating the thermal conductivity of the outlet gases of the reactor applied in the reduction experiments, an innovative method was developed to analyze experimental data and indirectly determine the overall degree of reduction. This work proposes a stepwise approach to extract kinetic parameters under conditions as close as possible to intrinsic by coupling experiments on micron-scale powders in thin fixed beds with a mathematical model capable of capturing the complexity of the reacting system. The experimental and modeled results were validated by analyzing solid samples from the experiments using various analytical techniques. The aim is to minimize interference from external mass and heat transfer and particle coalescence. The model serves as a tool for parameter identification at small scale, which is a prerequisite for model-based analysis and design of direct reduction processes using hydrogen. Developing an overall model based on accurate intrinsic kinetic parameters and subsequently incorporating transport phenomena leads to significantly better predictive and extrapolative capability compared to models relying on lumped parameters. This aspect is particularly critical for scale-up, as errors present at small scale tend to be amplified when transitioning to larger systems. For these reasons parameters obtained for powders are intended for future integration into pellet-level models (SCM or Grain Model with evolving porosity and tortuosity) and reactor-scale simulations of countercurrent furnaces.

2. Materials and methods

2.1. Materials

The solid samples used for the reduction experiments in this work were purchased from Sigma-Aldrich. Specifically, hematite (CAS: 1309-37-1) has a purity ≥96%, a density of 5.25 g/cm^3, and particle sizes smaller than 5 μm, while magnetite (CAS: 1317-61-9) has a purity ≥95%, a density ranging between 4.8 and 5.1 g/cm^3, and particle sizes below 5 μm.

The use of powders makes it possible to minimize phenomena that influence the reduction kinetics. Based on the evaluation of specific criteria, the mass and heat transfer limitations can therefore be considered negligible. The powders were characterized from multiple perspectives to assess particle size distribution, porosity, specific surface area and initial and transient chemical composition. These analyzes confirmed the theoretical and modeling assumptions used to evaluate the reduction kinetics. As for the gas phase, hydrogen (>99.999%), which was used as the sole reducing agent, and argon (Ar) (>99.9%), which served as an inert carrier gas, were supplied by Woikoski Oy.

2.2. Chemical and physical characterization

X-ray diffraction (XRD) was used to thoroughly analyze the evolution of the chemical species involved in the reduction of the pure iron oxides. Specifically, diffraction patterns in the 2θ range of 20–80° were collected using a Panalytical Empyrean XRD instrument equipped with a PIXcel 3D detector and CuKα radiation (1.5418 Å) as the source. Particle size distribution analysis (i.e., Light scattering, LS) was performed using a Malvern Panalytical MASTERSIZER 3000. Nitrogen physisorption measurements were performed using a Micromeritics 3Flex-3500 system to evaluate the porosity of the material as well as its specific surface area (i.e., BET method). Further analyses, such as thermogravimetry/differential scanning calorimetry coupled with mass spectrometry (i.e., TGA/DSC-MS), are described in more detail in D'Angelo et al. [37].

2.3. Experimental setup

The reduction experiments on both solid materials were performed under different operating conditions using an Autochem 2910 device. Although this apparatus is generally used for chemisorption studies on catalysts, it has also proven to be effective for studies on heterogeneous gas-solid reactions. The experimental setup is equipped with a thermal conductivity detector (TCD) for the analysis of off-gases, which allows very frequent and precise measurements (i.e., thermal conductivity values every 0.02 s) of the gas composition. The TCD works based on a classic Wheatstone bridge configuration. The system generates a signal by detecting the temperature change - and therefore the electrical resistance - of heated filaments in contact with the gas. The TCD signal is determined by comparing the thermal conductivity between a reference gas (Ar) and the gas mixture exiting the reactor, which contains Ar, H_2 and H_2O. This approach is particularly effective for hydrogen reduction studies, as the thermal conductivity of H_2 and the other gases differ significantly. As a result, the TCD signal can be interpreted as an indicator of the amount of unreacted hydrogen at the reactor outlet. The setup of the experimental system is shown in Fig. 2.

A fixed bed reactor configuration was adopted. High purity gases stored in cylinders (1) are fed at a controlled flowrate via flowmeters (2) and mixed before entering the reactor. The glass reactor (3) has a tubular geometry with a length (L) of 193 mm and a radius (R) of 11 mm. It is housed in a small furnace (4) which allows precise temperature control, which is monitored by a Type-K thermocouple (5) located in the center of the reactor near the fixed bed. The fine solid sample is loaded into the reactor and placed on a quartz disk resting on a layer of quartz wool (6). These porous layers serve to protect the detectors (7) from possible entrainment of solid particles by the gas flow and to ensure a horizontally flatbed geometry, minimizing non-uniform gas-solid interactions along the bed. The TCD signal and temperature data are finally recorded and extracted (8). The use of the TCD in this study is motivated by its practical suitability for monitoring H_2-based iron oxide reduction. While mass spectrometer (MS) and gas chromatography (GC) techniques provide species-specific detection, TCD offers a rapid, continuous and quantitative signal directly correlated with the reaction progress without species-dependent calibration. Its robustness under standard operating conditions and its limited sensitivity to background fluctuations make it particularly reliable. TCD is widely accessible in conventional gas-analysis setups and provides adequate sensitivity for detecting variations in H_2 concentration within H_2/H_2O systems. Moreover, its intrinsic tolerance to water vapor allows direct analysis of the gas stream produced during reduction, avoiding the need for extensive pretreatment typically required when MS or GC systems are exposed to significant amounts of moisture. These advantages make TCD a practical, reliable, and efficient tool for real-time kinetic monitoring in hydrogen-driven reduction studies.

To validate the use of the TCD for evaluating the reduction of iron oxide with H_2, an Agilent 990 Micro GC was used to evaluate the composition of the off gases. Fig. S1 (Supplementary Material) compares the TCD raw signal and Micro GC H_2 molar fraction profiles for the same experiment, illustrating consistent trends and validating the TCD-based approach.

Repeatability was verified through repeating the same experiment under identical conditions (Table 1, 2H); the comparative plot (Fig. S2) and all raw data (Figs. S3 and S4) are provided in the Supplementary Material. The repetition resulted in error bars below 1%, confirming the robustness of the measurements.

In all experiments, the solids were heated at a constant temperature ramp of 10 °C/min to ensure uniform thermal evolution across all samples. To accurately determine the kinetics of iron oxide reduction by H_2, a series of isothermal experiments were performed under different operating conditions. In particular, the effect of temperature (T), total volumetric gas flow rate (Q) and hydrogen molar fraction (y_{H_2}) was

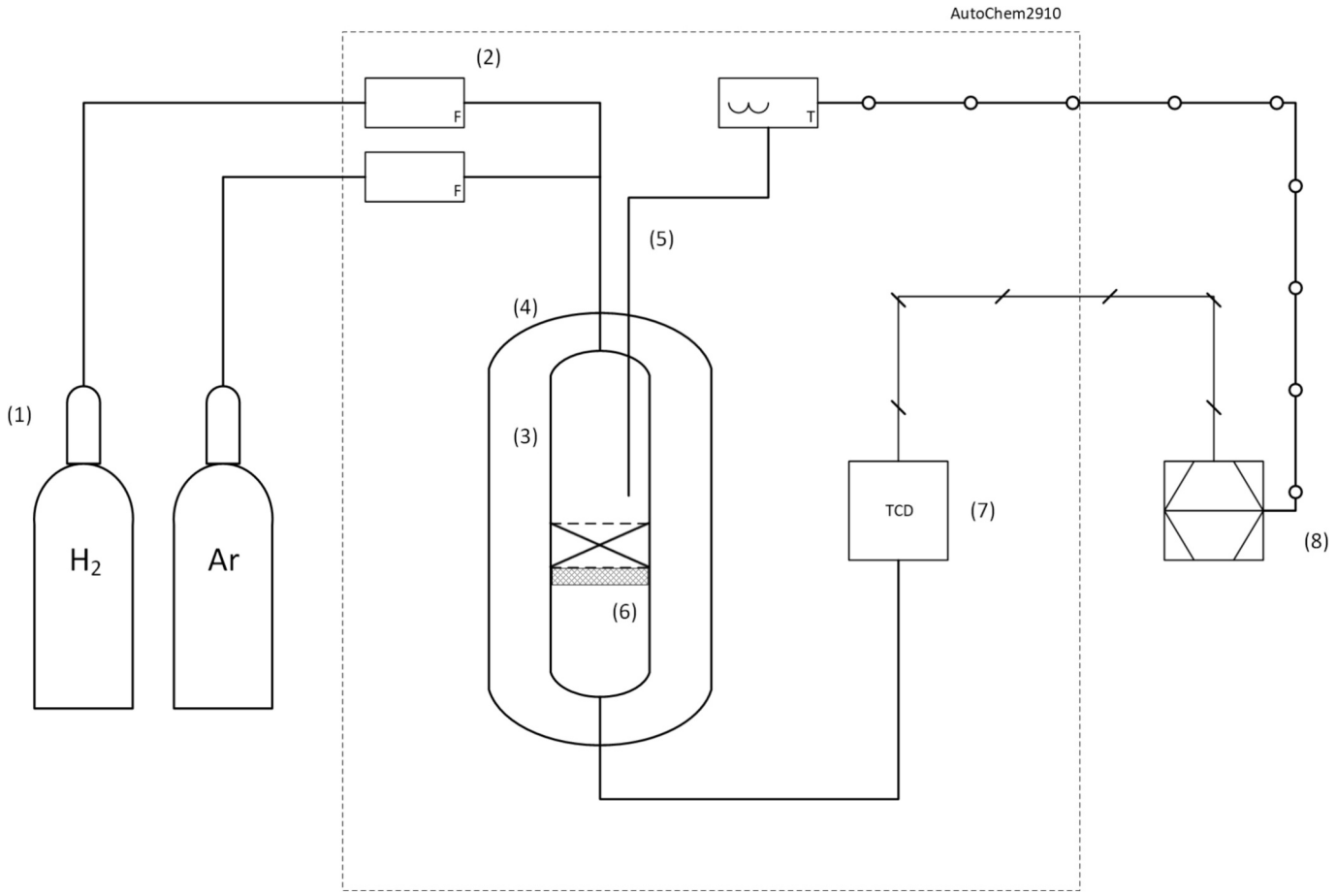

Fig. 2. Schematic of the thin solid reactor experimental setup: gases cylinders (1), flowmeters (2), reactor (3), furnace (4), thermocouple (5) inert support (6), detectors (7) and computer (8).

Table 1
Experimental conditions used for hematite and magnetite reduction.

Species	*Test*	T [°C]	Q_{H_2} [mL/min]	Q_{Ar} [mL/min]	Q [mL/min]	y_{H_2} [−]	*mass* [g]
Fe_2O_3	1H	600	3	17	20	0.15	0.0158
Fe_2O_3	2H	600	4	16	20	0.20	0.0133
Fe_2O_3	3H	600	5	15	20	0.25	0.0144
Fe_2O_3	4H	700	4	16	20	0.20	0.0133
Fe_2O_3	5H	800	4	16	20	0.20	0.0158
Fe_2O_3	6H	1000	4	16	20	0.20	0.0129
Fe_2O_3	7H	600	3	15	18	0.20	0.0129
Fe_2O_3	8H	600	5	19	24	0.20	0.0145
Fe_2O_3	9H	600	6	22	28	0.20	0.0138
Fe_3O_4	1M	600	3	17	20	0.15	0.0136
Fe_3O_4	2M	600	4	16	20	0.20	0.0153
Fe_3O_4	3M	600	5	15	20	0.25	0.0131
Fe_3O_4	4M	700	4	16	20	0.20	0.0139
Fe_3O_4	5M	800	4	16	20	0.20	0.0102
Fe_3O_4	6M	600	3	15	18	0.20	0.0129
Fe_3O_4	7M	600	5	19	24	0.20	0.0116
Fe_3O_4	8M	600	6	22	28	0.20	0.0133

investigated.

2.4. Mathematical and physical interpretation of TCD signals

Analyzing the thermal conductivity signal can be particularly challenging, especially when attempting to simulate the signal itself. This is because the signal not only reflects the conductivity difference between the reference gas and the exhaust gases but is also affected by the physical and structural properties of the Wheatstone bridge [64]. Despite this complexity, the high sensitivity of the acquired data allows for a unique interpretation of the reduction process. As an example, Fig. 3 shows the original thermal conductivity signal obtained during a hematite reduction experiment at 600 °C with a total gas flow rate of 20 mL/min and a hydrogen molar fraction in the feed of $y_{H_2} = 0.2$.

As can be seen, the signal increases within a few seconds of starting the test, which is due to the higher thermal conductivity of the reducing gas compared to the reference gas (Ar). It can be expected that the changes in signal slope are correlated with the different phases of the

Table 2
Fixed model parameters. *[44], **[68], *** [67].

Parameter	Value	Unit	Parameter	Value	Unit
$d_{1,1}^{*}$	$1 \bullet 10^{-4}$	m^2s^{-1}	$m_{2,2}^{*}$	0.50	–
$d_{2,1}^{*}$	3.43	–	$m_{3,2}^{*}$	$1.26 \bullet 10^{3}$	–
$d_{3,1}^{*}$	$4.2 \bullet 10^{3}$	K	$m_{4,2}^{*}$	$-1.96 \bullet 10^{5}$	–
$d_{1,2}^{*}$	$1 \bullet 10^{-4}$	m^2s^{-1}	$m_{1,3}^{*}$	$8.39 \bullet 10^{-7}$	Pa s
$d_{2,2}^{*}$	5.64	–	$m_{2,3}^{*}$	0.62	–
$d_{2,3}^{*}$	$6.8 \bullet 10^{3}$	K	$m_{3,3}^{*}$	75.38	–
$d_{1,3}^{*}$	$1 \bullet 10^{-4}$	m^2s^{-1}	$m_{4,3}^{*}$	− 432.5	–
$d_{2,3}^{*}$	4.77	–	ν_1^{***}	7.07	–
$d_{3,3}^{*}$	$5.9 \bullet 10^{3}$	K	ν_2^{***}	12.7	–
$m_{1,1}^{*}$	$1.56 \bullet 10^{-7}$	Pa s	ν_3^{***}	18	–
$m_{2,1}^{*}$	0.71	–	ε	0.1	–
$m_{3,1}^{*}$	− 5.87	–	Pe	12	–
$m_{4,1}^{*}$	210	–	L	0.18	m
$m_{1,2}^{*}$	$2.70 \bullet 10^{-6}$	Pa s	R	$5.50 \bullet 10^{-3}$	m

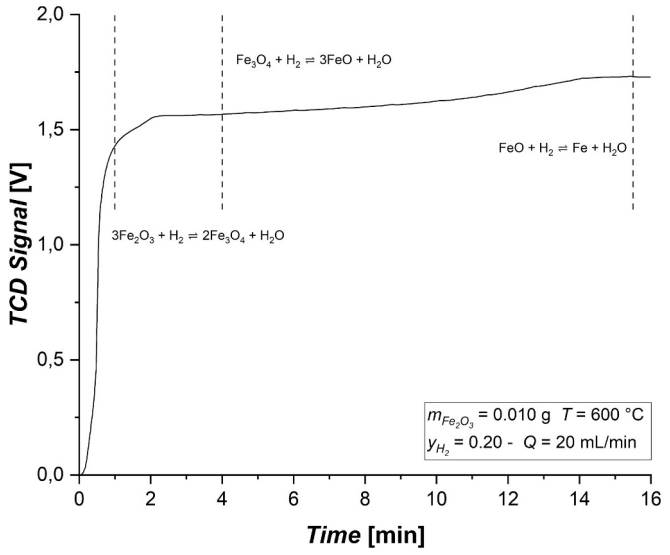

Fig. 3. Example of TCD signal; experimental conditions: $m_{Fe_2O_3} = 0.010\,g, T = 600^{\circ}C, y_{H_2} = 0.20, Q = 20\,mL/min$.

reaction and are therefore likely caused by the nature of the reactive network. These slope changes may thus indicate shifts in the kinetic or thermodynamic regime caused by the depletion of solid chemical species that previously dominated the reaction. The first major slope change, which occurs after a few minutes, can be interpreted as the almost complete reduction of Fe_2O_3, which is known in the literature as the fastest step and is not limited by thermodynamics (Fig. 1). According to this interpretation, the subsequent changes in the slope correspond to the approach of the next reduction step or a shift in the dominant chemical species consuming H_2, depending on its kinetics as well as diffusion and thermodynamic constraints. To verify these assumptions, stop tests were conducted under the same operating conditions, where the reaction was stopped after 5 min, 10 min, 50 min and beyond. The XRD analysis of the samples collected confirmed these assumptions and showed a direct correlation between the acquired signal and the conversion of the solids in the reactor. However, as mentioned above, the simulation of the signal itself (and not the intrinsic thermal conductivity of the exhaust gas) is complex. Since the signal is mainly influenced by hydrogen, an alternative approach was proposed, correlating the gas-derived signal with an indirect estimate of the overall sample reduction degree. To this end, several mathematical transformations were applied to the measurement. Fig. 4 illustrates the numerical processing step by step (from A to D) leading to the result.

The procedure starts with an initial normalization of the data (A); under certain conditions, the normalized signal alone can represent the thermal conductivity of the analyzed gasses [64]. This enables the second step, taking the complement (of one) of the signal (B), which is useful for integral calculation. Step C is crucial as it involves a cumulative integral of the complement signal point by point using the trapezoidal method, yielding a signal in (D) that reflects the reduction curves reported by several authors in thermogravimetric studies [65]. However, particularly in the early stages of the reaction, the hydrogen reaching the detector corresponds to the H_2 supplied due to dilution effects (i.e., axial dispersion). This leads to an overestimation of the degree of conversion, since the integral contains both the hydrogen that has reacted in the sample and the fraction that has not reached the detector due to physical effects.

As will be shown later in the Results section, the fluid dynamics of the reactor were evaluated using a residence time distribution (RTD) analysis, which revealed that the system did not behave like an ideal plug flow reactor. In order to accurately evaluate the data, the integral had to be corrected by the blank signal (i.e., from an experiment in the absence of the solid sample) under the same operating conditions. Fig. 5a shows an example of the overlap between the blank TCD signal and the result of a reduction test. The difference, highlighted in blue, is considered for producing a corrected normalized TCD signal to be treated by the procedure outlined above, yielding a significantly different estimate of the reduction degree (Fig. 5b).

The area to be considered, which represents the actual H_2 consumption by the chemical reaction, lies between the two curves (Fig. 5a). By subtracting the cumulative integrals, the corrected final result is obtained, which is no longer overestimated. Signal processing was carried out using deterministic mathematical operations – normalization, complement transformation, cumulative integration, and blank subtraction – based on the intrinsic properties of the TCD signal, without empirical filtering or arbitrary smoothing. The inherent stability of the TCD signal eliminates issues related to baseline drift or offset definition, ensuring greater robustness. Blank subtraction was synchronized with experimental timing (valve opening) to minimize alignment artefacts.

This value can then be compared with the actual global reduction degree of the solid sample and used to estimate the kinetic parameters of the multistage reduction of iron oxides. The most important innovation is the means to correlate the raw data — measured with a very accurate gas detector— with the degree of conversion of a solid in heterogeneous gas-solid reactions. This is confirmed in the present work not only by the accurate fit of the experimental data, but also by an accurate physicochemical interpretation provided by the model of the reactive system.

2.5. Mathematical model

The mathematical model developed in this study to evaluate the reduction kinetics of pure iron oxides represents a more rigorous and detailed version of a model previously presented by the authors [66]. The main differences lie in a more detailed assessment of the mass balance of the chemical reaction, which takes into account the particle size distribution of the solid, in a more realistic behavior of the reaction fronts and in a more detailed treatment of the gas-phase fluid dynamics within the full and empty volume of the reactor. The proposed model combines a classical axial dispersion approach with a dynamic shrinking core model (SCM) that includes the product layer approach. The thin fixed bed, which is discretized vertically into a grid of 20 points in the model, reacts in each layer according to sequential reaction dynamics evolving from a single reaction front to three fronts and then back to one front in the particles. At each time step, the model dynamically evaluates the state of the solids in each layer and selects the appropriate set of equations based on the number of reaction fronts. In this way, a wide range of phenomena are taken into account, including kinetics, thermodynamics as well as external and internal diffusion effects. On the solid side, the model assumes radial homogeneity of all structural,

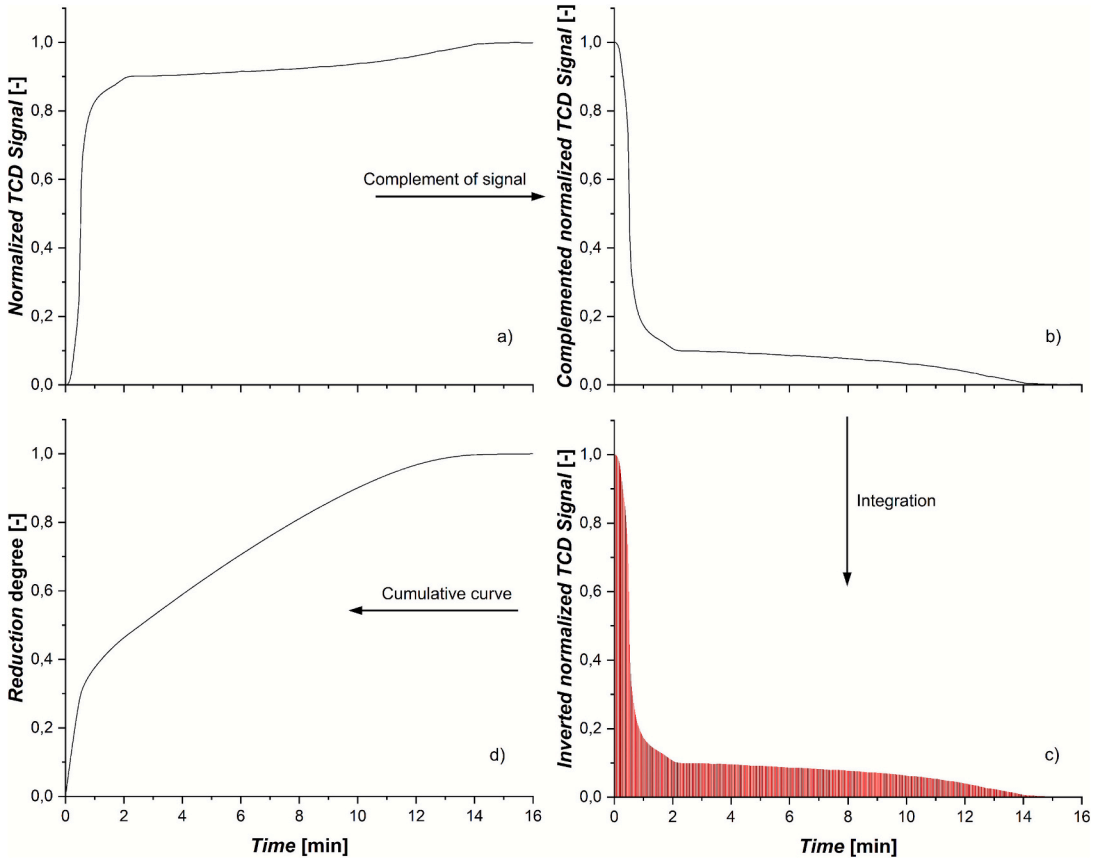

Fig. 4. Numerical elaboration of TCD signal raw data: a) Normalized TCD signal; b) Complement of normalized TCD signal; c) Integration of the complement signal; d) reduction degree obtained from cumulative integration.

compositional, and porosity-related properties of the layers. On the gas side, a constant total gas concentration within the particles at uniform temperature and pressure within the particles as well as a quasi-steady state (i.e., no accumulation of gas phase species) are assumed. In the model a reaction takes place exclusively at the interface between two distinct solid regions: an unreacted inner core and a surrounding shell of reacted material. As the core is being consumed, the surface area of the reaction front gradually decreases. The different remaining product layers are always considered in the context of intraparticle diffusion phenomena that describe the reaching the reaction front or product gases that the exit. In the reaction network considered in this study, a maximum of three different reaction fronts is considered.

2.5.1. Gas mass balance

The gas-phase mass balance equations describe the evolution over time (t) of the concentrations of reducing and oxidizing agents in the reactor. The gas-phase model includes convection, axial dispersion and a reaction term that is governed by dynamic SCM. Based on the reactor length L and the height of the solid bed h, two dimensionless axial co-ordinates, z_1 and z_2, are defined to identify the two reactor zones: the empty zone ($l = 1$) (convection and dispersion) and the reactive zone ($l = 2$) (gas flow and chemical reactions). In the system of differential equations, subscript i refers to the gas phase species (i.e., H_2 and H_2O), while j represents the reaction or reaction front under consideration: $j = 1$ for the first reduction (hematite to magnetite), $j = 2$ for the second (magnetite to wüstite), and $j = 3$ for the third one (wüstite to metallic iron).

$$\frac{\partial c_i(t,z_l)}{\partial t} = \begin{cases} -\frac{u}{L-h}\cdot\frac{\partial c_i(t,z_1)}{\partial z_1} + \frac{D_z}{(L-h)^2}\cdot\frac{\partial^2 c_i(t,z_1)}{\partial {z_1}^2} & \text{for } l=1 \\ -\frac{u}{h}\cdot\frac{\partial c_i(t,z_2)}{\partial z_2} + \frac{\partial^2 c_i(t,z_2)}{\partial {z_2}^2} + (1-\varepsilon)\cdot\sum_{j|_f}^{3}\nu_{i,j}\cdot r_j(t,z_2) & \text{for } l=2 \end{cases} \quad (1)$$

In this equation, c_i is the concentration of the i:th gas species, while $\nu_{i,j}$ are the stoichiometric coefficients of the i:th gas species in reaction j. The boundary conditions of the PDE system are defined at the reactor inlet ($z_1 = 0$), at the outlet of the empty zone ($z_1 = 1$), at the inlet of the reactive bed ($z_2 = 0$) and at the system outlet ($z_2 = 1$).

$$c_i(t,z_1)\,|_{z_1=0} = c_{i,\text{in}} \qquad \left.\frac{\partial c_i(t,z_1)}{\partial z_1}\right|_{z_1=1} = 0 \quad (2)$$

$$c_i(t,z_2)\,|_{z_2=0} = c_i(t,z_1)\,|_{z_1=1} \qquad \left.\frac{\partial c_i(t,z_2)}{\partial z_2}\right|_{z_2=1} = 0 \quad (3)$$

As for the geometric and fluid dynamic parameters, h is the theoretical height of the fixed bed; u is the superficial gas velocity and D_z is the axial dispersion coefficient. These parameters are calculated using

$$h = \frac{V_s}{S} = \frac{m_s}{\rho\cdot\pi R^2} \quad (4)$$

$$u = \frac{Q}{S} = \frac{Q_0}{S}\cdot\frac{T}{T_0}\cdot\beta \quad (5)$$

$$D_z = \frac{L\cdot u}{Pe} \quad (6)$$

S is the cross-sectional area of the reactor (derived from the inner

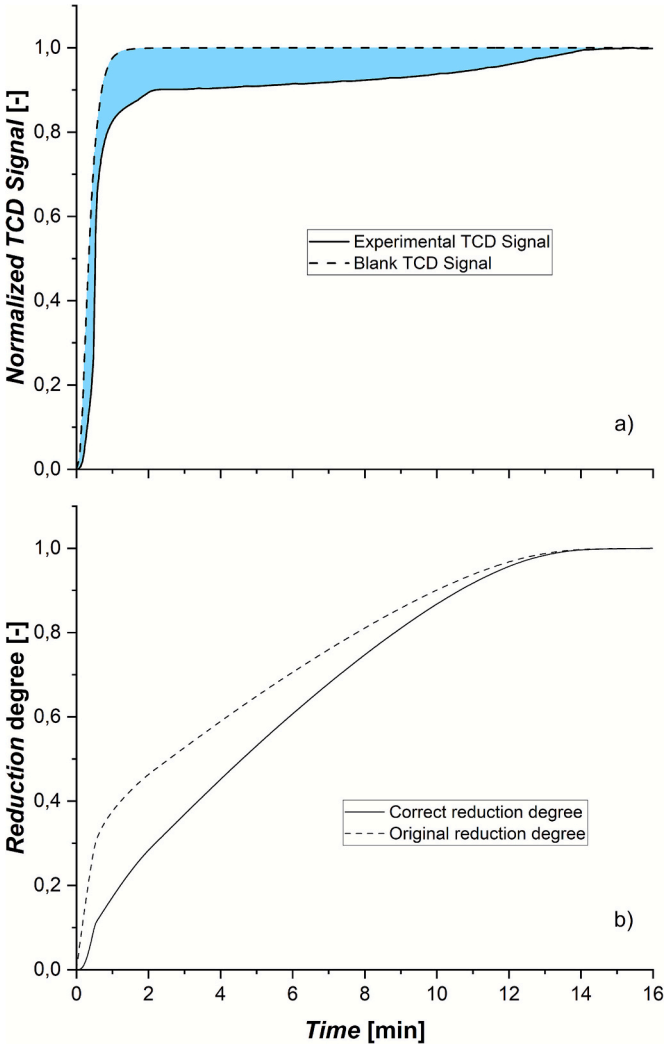

Fig. 5. Numerical correction of the reduction degree from TCD signal raw data: a) difference between the TCD signals in the blank and reduction experiments (blue region), and b) original (solid line) and corrected (dashed line) reduction degrees.

radius R), and V_s is the theoretical volume of the loaded sample obtained as the mass-to-density ratio of the iron oxide. The gas velocity is defined as the ratio of the actual volumetric flow rate Q to S, where Q is derived from the volumetric flow rate at standard conditions (Q_0), adjusted by the operating temperature T and the reference temperature $T_0 = 295$ K and converted using the factor $\beta = 10^{-6}/60$ (m^3/min)/(dm^3/s). The axial dispersion coefficient D_z is calculated based on its definition using the Peclet number (Pe). The fluid dynamics and the Peclet number were evaluated experimentally by residence time distribution (RTD) tests (see Results section). Finally, ε is the initial bed void fraction experimentally determined by physisorption experiments. For the reactive term, the reduction rate r_j is given by

$$r_j(t,z_2) = \sum_{n=1}^{N} x_n \bullet \frac{P}{R_g T}\frac{3}{r_n^0}\frac{1}{A_j(t,z_2,r_n^0)\,|_f}\cdot\left(\frac{N_j(t,z_2,r_n^0)\,|_f}{W(t,z_2,r_n^0)\,|_f} - y_{H_2,j,eq}(t,z_2)\right) \tag{7}$$

R_g is the gas constant, P representa the operating pressure and $y_{H_2,j,eq}$ is the equilibrium molar fraction of the reducing agent for reaction j. The global reduction rate is calculated by weighing each reaction rate by the initial radius r_n^0 of each particle size class and their respective weight fraction x_n. With this approach, the contribution of the individual particle size classes to the overall reduction process can be evaluated. The particle size distributions of the hematite and magnetite samples are presented in the Results section. To properly evaluate the driving force of each reaction front, $y_{H_2,j,eq}$ is evaluated for the j:th reaction as

$$y_{H_2,j,eq}(t,z_2) = \frac{1}{1+K_j}\cdot\left(y_{H_2,j}(t,z_2) + y_{H_2O,j}\left(t,z_2\right)\right) \tag{8}$$

where $y_{i,j}$ represents the molar fraction of the gas species over time and position within the bed while K_j is the equilibrium constant of the j:th reaction.

Variables A_j, N_j and W are crucial for describing how the model dynamically describes the progress of the reduction and selects the appropriate number of analytical equations. For example, if X_j is defined as the degree of conversion of an oxide ($j = 1$ Fe_2O_3, $j = 2$ Fe_3O_4, $j = 3$ FeO) with hematite as the starting material, the interaction between the reducing gas and the solid initially defines the first and only active reaction front with $X_1(t,z_2) = 0$ ($f = 1$). If a layer satisfies both the conditions $X_1(t,z_2) < 1$ and $X_2(t,z_2) = 0$, two reaction fronts become active. A third front appears if $X_1(t,z_2) < 1$ and $X_2(t,z_2) < 1$. Conversely, the number of active fronts decreases when $X_j(t,z_2) = 1$, which indicates that the oxide in question has been completely converted in this layer. As a result, W and N_j vary depending on the number of active reaction fronts. The parameter f changes its value based on the model's self-assessment, according to the scheme

$$\text{if}\begin{cases} X_1(t,z_2)=0 & f=1 \quad j=1 \\ X_1(t,z_2)<1 \wedge X_2(t,z_2)=0 & f=2 \quad j=1,2 \\ X_1(t,z_2)<1 \wedge X_2(t,z_2)<1 \wedge <0\, X_3(t,z_2)<1 & f=3 \quad j=1,2,3 \\ X_1(t,z_2)=1 \wedge X_2(t,z_2)<1 \wedge X_3(t,z_2)<1 & f=2 \quad j=2,3 \\ X_1(t,z_2)=1 \wedge X_2(t,z_2)=1 \wedge X_3(t,z_2)<1 & f=1 \quad j=3 \\ X_1(t,z_2)=1 \wedge X_2(t,z_2)=1 \wedge X_3(t,z_2)=1 & f=0 \end{cases} \tag{9}$$

N_j here denotes the effective reduction rate for the j:th front, while W represents the total resistance for mass transfer and reaction. These are calculated using the parameters A_j, B_j and F, which represent kinetic resistances, intraparticle diffusion resistances and external diffusion resistances, respectively, according to

$$\begin{aligned} N_1\left(t,z_2,r_n^0\right)\,|_3 = {} & (A_1A_2A_3)\cdot y_{H_2,1} + [A_1A_2(B_3+F)]\cdot y_{H_2,3,eq} \\ & + [A_1A_3B_2 + A_1A_3(B_3+F) + A_1B_2(B_3 \\ & + F)]\cdot y_{H_2,2,eq} + [A_3B_1(A_2+B_2) + A_3B_1(A_2 \\ & + B_2) + B_1(A_2+B_2)(B_3+F) + A_2A_3B_2 + A_2A_3(B_3+F) \\ & + A_2B_2(B_3+F)]\cdot y_{H_2,1,eq} \end{aligned} \tag{10}$$

$$\begin{aligned} N_2\left(t,z_2,r_n^0\right)\,|_3 = {} & [A_2A_3(A_1+B_1)]\cdot y_{H_2,2} + [A_2(A_1+B_1)(B_3+F)]\cdot y_{H_2,3,eq} \\ & + [A_3(A_1+B_1)(B_3+F) + B_2(A_1+B_1)(B_3+F) \\ & + A_3B_2(A_1+B_1)]\cdot y_{H_2,2,eq} + [A_2A_3B_2 + A_2A_3B_2 \\ & + A_2B_2(B_3+F) + A_2A_3(B_3+F)]\cdot y_{H_2,1,eq} \end{aligned} \tag{11}$$

$$\begin{aligned} N_3\left(t,z_2,r_n^0\right)\,|_3 = {} & [A_3(A_1+B_1)(A_2+B_2) + A_2A_3B_2]\cdot y_{H_2,3} + [(A_1 \\ & + B_1)(A_2+B_2)(B_3+F) + A_2B_2(B_3+F)]\cdot y_{H_2,3,eq} \\ & + [A_3(A_1+B_1)(B_3+F)]\cdot y_{H_2,2,eq} + [A_2A_3(B_3 \\ & + F)]\cdot y_{H_2,1,eq} \end{aligned} \tag{12}$$

$$W(t,z_2,r_n^0)\,|_3 = \Big\{ (A_1+B_1)\cdot[A_3(A_2+B_2+B_3+F)+(A_2+B_2)\cdot(B_3+F)]+A_2[A_3(B_2+B_3+F)+B_2(B_3+F)] \Big\}\cdot y_{H_2,1,eq} \tag{13}$$

$$N_2(t,z_2,r_n^0)\,|_2 = (A_2A_3)\cdot y_{H_2,2}+[A_2(B_3+F)]\cdot y_{H_2,3,eq}+[A_2B_1+(A_3+B_2)(B_3+F)]\cdot y_{H_2,2,eq} \tag{14}$$

$$N_3(t,z_2,r_n^0)\,|_2 = A_3(A_2+B_2)\cdot y_{H_2,2}+[(A_2+B_2)(B_3+F)]\cdot y_{H_2,3,eq}+[A_3(B_3+F)]\cdot y_{H_2,2,eq} \tag{15}$$

$$W(t,z_2,r_n^0)\,|_2 = A_3(A_2+B_2+B_3+F)+(A_2+B_2)\cdot(B_3+F) \tag{16}$$

$$N_3(t,z_2)\,|_1 = y_{H_2,3}(t,z_2)-y_{H_2,3,eq}(t,z_2) \tag{17}$$

$$W(t,z_2,r_n^0)\,|_1 = \frac{A_3+B_3+F}{A_3} \tag{18}$$

The analytical expressions for these variables vary depending on the number of active fronts. For oxides other than hematite — where all three reaction fronts may occur at some point — the same modeling approach applies to experiments starting from Fe_3O_4 or FeO, with fewer maximum fronts. A_j, B_j and F are defined as

$$A_j(t,z_2)\,|_f = \frac{1}{(1-X_j(t,z_2))^{\frac{2}{3}}}\cdot\frac{1}{k_j\cdot\left(1+\frac{1}{K_j}\right)} \tag{19}$$

$$B_j(t,z_2,r_n^0)\,|_f = \frac{(1-X_{j+1}(t,z_2))^{\frac{1}{3}}-(1-X_j(t,z_2))^{\frac{1}{3}}}{(1-X_j(t,z_2))^{\frac{1}{3}}\cdot(1-X_{j+1}(t,z_2))^{\frac{1}{3}}}\cdot\frac{r_n^0}{D_j};\quad X_{j+1}(t,z_2)=0 \ \text{ if } j+1>\max(j)\Big|_f \tag{20}$$

$$F = \frac{1}{H} \tag{21}$$

where k_j is the kinetic constant, D_j is the intraparticle diffusion coefficient and H is the external mass transfer coefficient. The kinetic parameters were determined by fitting experimental reduction data using the linearized Arrhenius equation, while the thermodynamic [8] and diffusion parameters [44] were obtained from established theoretical and empirical expressions (Table 2).

$$k_j = k_{j,ref}\bullet\exp\left[\left(-\frac{E_{a,j}}{R}\right)\bullet\left(\frac{1}{T}-\frac{1}{T_{ref}}\right)\right] \tag{22}$$

$$K_j = \exp\left(-\frac{\Delta G_j}{RT}\right) \tag{23}$$

$$D_j = d_{1,j}\bullet\exp\left(d_{2,j}-\frac{d_{3,j}}{T}\right) \tag{24}$$

$k_{j,ref}$ and $E_{a,j}$ are the pre-exponential factor and the activation energy, respectively, while T_{ref} is the reference temperature (600 °C). ΔG_j is the change in Gibbs free energy calculated from the changes in enthalpy (ΔH_j) and entropy (ΔS_j) of the reactions. The terms $d_{1,j}$, $d_{2,j}$ and $d_{3,j}$ are coefficients used in the equation to describe intraparticle diffusion.

2.5.2. Solid mass balance

The solid phase mass balances of the different iron oxides are described as functions of time and position z along the axial coordinate of the reactive bed

$$\frac{\partial X_j(t,z_2)}{\partial t} = (1-\varepsilon)\frac{r_j(t,z_2)}{n_0\cdot a_j} \tag{25}$$

where n_0 represents the initial oxygen content (e.g., $n_0 = 3m/M_{Fe_2O_3}$) of the sample, while a_j is the proportional oxygen content function of the type of iron oxide.

The overall degree of reduction of the solid is therefore calculated by

$$X(t,z_2) = \sum_j^3 a_j \bullet X_j(t,z_2) \tag{26}$$

The average degree of reduction ($\overline{X}_s$), calculated along the z_2, was used for comparison with the experimental data in the objective function during parameter estimation (Section 2.5.5).

2.5.3. Phenomenologies negligible by criterion

Regarding external diffusion phenomena, the particle size distribution provided by the supplier and later refined through DLS techniques suggests that such mass transport limitations can be reasonably neglected. The external mass transfer coefficient, denoted as H, was calculated under varying operating conditions and for all particle size families. It is given by

$$H = Sh\cdot\frac{D_{mol}}{2r_n^0} \tag{27}$$

where Sh is the Sherwood number and D_{mol} is the molecular diffusivity. The Sh value is estimated using classical correlations involving the Schmidt (Sc) and Reynolds (Re) numbers, through

$$Sh = 2+0.6Re^{1/2}Sc^{1/3} \tag{28}$$

$$Sc = \frac{\mu_g}{\rho_g\cdot D_{mol}} \tag{29}$$

$$Re = \frac{2Ru\cdot\rho_g}{\mu_g} \tag{30}$$

The molecular diffusivity was calculated using the formulation proposed by Valipour et al. [67]

$$D_{mol} = \frac{1\cdot10^{-7}\cdot T^{1.75}}{P\cdot\left(\sum v_i^{1/3}\right)^2}\cdot\left(\sum\frac{1}{M_i}\right)^{1/2} \tag{31}$$

where v_i represent the diffusion volumes of the gas species involved (Table 2). Finally, μ_g and ρ_g represent the viscosity and density of the gas, respectively, calculated as

$$\rho_g = \frac{P\cdot\sum y_iM_i}{R_gT} \tag{32}$$

$$\mu_g = \sum y_i\mu_i;\qquad \mu_i = \frac{m_{1,i}\cdot(T/K)^{m_{2,i}}}{1+\frac{m_{3,i}}{(T/K)}+\frac{m_{4,i}}{(T/K)^2}} \tag{33}$$

coefficients m_i are derived from an empirical equation obtained via

CHEMCAD [68]. The detailed and quantitative evaluation of the mass transfer coefficient H revealed an average value of approximately 1000 m/s, confirming that the external mass transfer resistance can be neglected when compared to the other resistances considered in the SCM model. In this study, the energy balance for the reduction of iron oxides with hydrogen was not considered, although the entire reaction network is endothermic. This choice is justified by the operating conditions describing the reduction of small beds of very fine particles where temperature gradients can be considered negligible if a strong external heat source is used to keep the temperature constant. To support this assumption theoretically, a criterion was adopted

$$T_j^{\text{center}} - T_j^{\text{surface}} = \frac{D_j\left(-\Delta H_j\right)}{\lambda_j} \cdot \left(c_{H_2}^{\text{surface}} - c_{H_2}^{\text{center}}\right) \tag{34}$$

where λ_j are the thermal conductivity coefficients of the reacting oxides [69]. The first term on the right side of the equation was evaluated to be always less than 1 K m^3 mol^{-1} ($5{\cdot}10^{-2}$ to $1{\cdot}10^{-1}$ K m^3 mol^{-1}) for all solids involved. The second term was evaluated using a worst-case scenario, assuming the highest hydrogen concentration at the surface (about 14 mol/m^3 at 873 K) and zero in the particle core. Based on this assessment, intraparticle temperature variations of −0.649 K for hematite, 1.61 K for magnetite and 1.23 K for wüstite were found. These results confirm the assumption of negligible internal temperature gradients, which is also supported by recent experimental evidence from Hessling et al. [70] in the case of much larger pellets.

2.5.4. Reaction front control

In heterogeneous gas–solid reactions, the reaction kinetics generally depend on the composition of the gas phase, while the solid phase usually only plays an indirect role, allowing the degree of conversion to be calculated. To accurately determine the kinetic parameters governing the reduction of iron oxides, it is necessary to prevent the mathematical model from selecting combinations during parameter estimation that match the data but give theoretically incorrect results. This is the case with sequential reaction fronts, where in the SCM an outer front can progress faster than an inner front, which can lead to an overlap or, in the worst-case scenario, a crossing of the fronts — situations that are physically inadmissible. To solve this problem, a mathematical means was developed to control the reaction front. For each integration step of the model, it calculates the hypothetical value of the subsequent reduction. Based on the derivative value $dX_j(t,z)/dt$ at a certain time t, the model estimates the future term using the trapezoidal method $dX_j(t+\Delta t,z)/dt$ where Δt is the maximum integration step defined by the numerical solver of the model. If the calculated degree of reduction of the outer front at time $t+\Delta t$ exceeds that of the adjacent inner front, the code forces the derivatives to be equal. This means that if an outer front moves faster than an inner front and could potentially overtake the latter, the two fronts are instead forced to advance at the same rate.

The key condition for front control is

$$X_j(t+\Delta t,z) = X_{j+1}(t+\Delta t,z) \quad \text{if} \quad X_{j-1}(t+\Delta t,z) < X_j(t+\Delta t,z) \tag{35}$$

2.5.5. Numerical solution

The mathematical model was developed in Matlab 2024a, where the system of partial differential equations was solved using the finite difference method. The backward scheme was used for the evaluation of the first-order spatial derivative and the centered scheme for the second-order spatial derivative. The two axial coordinates of the reactor were discretized into 20 nodes each. The resulting system of ordinary differential equations was solved with the function *ode15s*, a solver of variable step size and variable order based on numerical differentiation formulas of order between 1 and 5. The parameter estimation was performed with *patternsearch*, a direct optimization algorithm belonging to the class of derivative-free methods. It is a deterministic solver based on a pattern search method in which the algorithm explores the solution space using a grid (pattern) and adapts this grid according to the optimization progress. The objective function used to minimize the distance between experimental data and the average simulated value of the thin layer over time ($\overline{X}_s$) is the following expression.

$$O = \sum_s^S \left(\frac{X_{\text{meas},s} - \overline{X}_s}{X_{\text{meas},s}}\right)^2 \tag{36}$$

Finally, the values and units of all model parameters are reported in Table 2.

3. Results

3.1. Materials characterization

In order to follow the development of the chemical reaction over time, a detailed analysis of the composition of the fixed bed was conducted using stop tests. The same reduction experiment was repeated several times under identical operating conditions, whereby the reaction was stopped at different times and corresponding samples were taken. Due to the minimum sample mass required for successful XRD analysis (> 70 mg), the experiments were performed with an initial solid mass of approximately 300 mg. Apart from the mass, all other operating conditions were identical to those specified in Table 1 for the standard test, which serves as a common reference point for all studies on the specific operating effects on the process (i.e., test 2H/M). The standard test was carried out at a temperature of 600 °C, a hydrogen molar fraction of 0.2 (balanced with argon as inert gas) and a total flow rate of 20 mL/min. When examining the reduction of a bed of pure hematite, the normalized thermal conductivity signal shows much sharper and more pronounced slope changes compared to the thin layer counterpart. A major challenge in this analysis lies in the complex interdependence of the signal, which is influenced by overlapping compositions in different bed layers and potential thermodynamic limitations due to hydrogen starvation and high vapor concentration in certain parts of the reactive bed. For this reason, this kinetic study propose a simplified analysis for thin bed layers — assuming a homogeneous composition throughout — avoiding increased complexity related to the influence of additional phenomena on the reduction behavior. The normalized thermal conductivity signal and the XRD results of the starting material and the intermediate samples are shown in Fig. 6.

The analysis confirmed that the starting material is pure hematite with rhombohedral structure crystallizing in the $R\bar{3}c$ space group. The stop tests conducted after 5 min, 10 min, 50 min and 150 min reveal the evolution of the fixed bed composition over time. These points were selected based on the overall behavior of the TCD signal to capture the reactor state just before and after the main slope transitions as well as during the slowest phase of the reduction (i.e., 150 min). It was observed that Fe_3O_4 appears very early and that Fe_2O_3 is almost completely depleted within the first 10 min, supporting the hypothesis that the slope changes in the TCD signal are directly related to the dominant solid-phase species and its control over the reaction regime. Before 50 min, another change in slope is observed, and the test stop after this time reveals the complete disappearance of Fe_2O_3 and the formation of FeO. In addition, the peaks associated with metallic iron begin to appear. After 150 min, wüstite appears to be the dominant phase promoting the final formation of metallic iron. The presence of magnetite in this phase can be partly explained by the disproportionation reaction of FeO into magnetite and metallic iron [60] that can occur during the cooling phase of the reactor. This cooling was carried out at a moderate ramp rate for technical and safety reasons, as it is not possible to rapidly quench a glass reactor system from operating to ambient temperature. The most important result of this analysis is not only the confirmation of the sequential nature of the reduction — as widely reported in the literature — but also the correlation of the gas phase signal with the evolution of the composition in the solid phase. While the size distribution of the

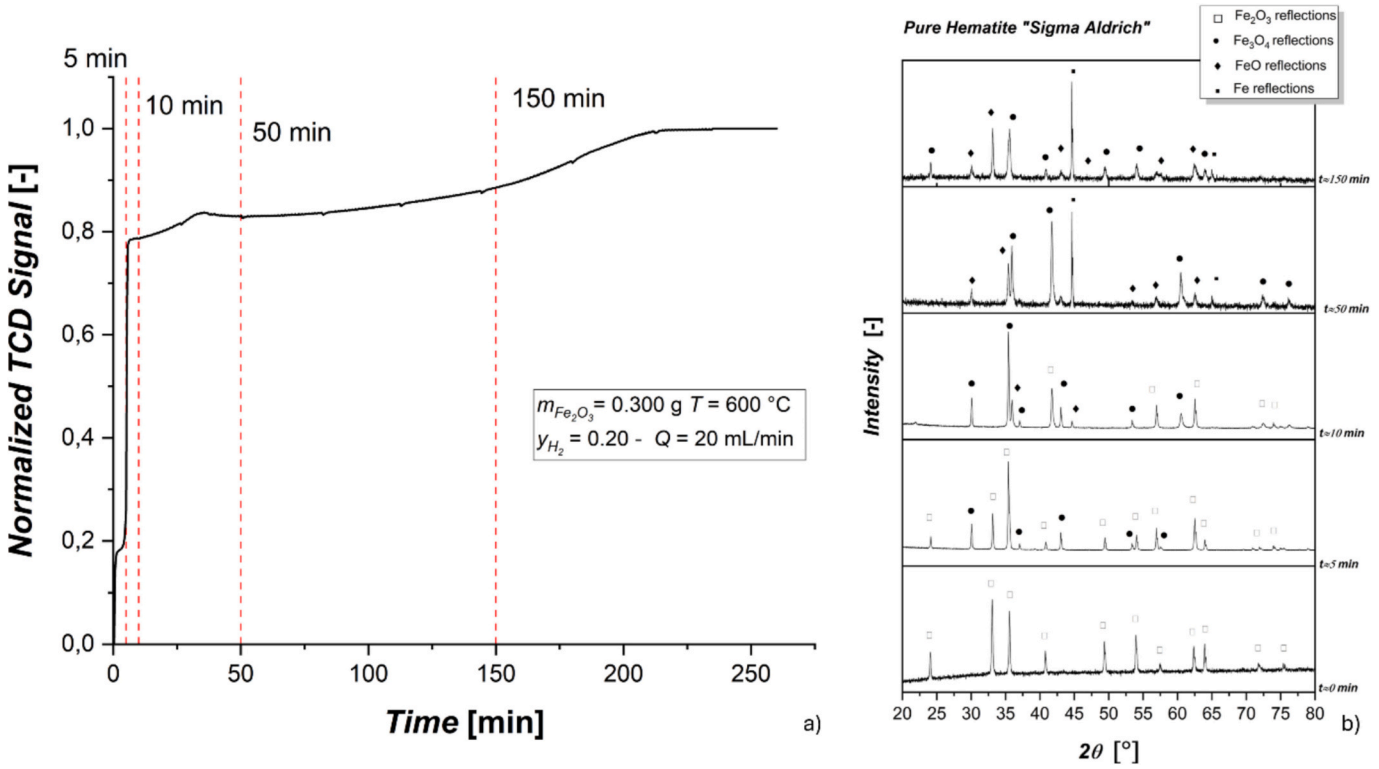

Fig. 6. a) Normalized TCD signal with marked stop points; b) XRD diffractograms of stop-test samples. Experimental conditions: $m_{Fe_2O_3} = 0.300$ g, $T = 600^{\circ}$C, $y_{H_2} = 0.20$, $Q = 20$ mL/min.

powder is usually provided by the manufacturer, a more detailed knowledge of the granulometric families is crucial to accurately evaluate the reaction rate using the dynamic SCM approach. Therefore, detailed LS analyses were performed to assess the particle size distribution. Fig. 7 shows the particle volume fractions for hematite and magnetite and cumulative distribution curve calculated based on $\log_{10}(2r_n^0)$ (order of magnitude 10^{-6} m). To evaluate the presence of phenomena such as agglomeration and coalescence of the particles, the LS technique was also used to analyze the grain size distribution of the reduced iron obtained from both hematite powder and pure magnetite. The results reported in Fig. S5 (Supplementary Material) show that in both cases the differences between the starting material and the reduced iron are negligible.

The results show significant differences. Hematite (Fig. 7a) has a narrow and well-defined size distribution with an average diameter between 1 μm and 2 μm. In contrast, magnetite has a much broader distribution, which partly contradicts the particle size of <5 μm stated by the manufacturer for both samples. Some magnetite particles reach a diameter of up to 100 μm, probably due to agglomeration. This result is critical as the reaction kinetics are strongly influenced by the particle size distribution, especially for the less oxidized form of iron where mass transport limitations may occur. Nitrogen physisorption measurements on the starting materials previously heated to 600 °C and evaluated using the BET method provided essential information about the surface area and porosity (ε). The initial porosity was found to be 0.1 for both samples [37].

3.2. Experimental results

The kinetic study of the reduction of a thin iron oxide layer under different operating conditions was carried out to evaluate the kinetic parameters of the individual reduction steps and to determine the control regimes of the process. The experimental investigations were performed by varying the operating temperature, the hydrogen content of the reduction gas and the total volumetric flow rate. The same experimental conditions were used for both pure hematite and pure magnetite powder. The model-based results obtained by parameter estimation, together with the experimental data processed using the integration and blank test correction method (cf. Materials and Methods), demonstrate that the mathematical model can accurately describe the overall reduction behavior determined based on the thermal conductivity of the outgoing gas flow.

As previously mentioned, the TCD signal primarily reflects the hydrogen content in the outlet gas, and the slope variations in the curves are closely related to the controlling regime as well as to the thermodynamics of the chemical reactions. This behavior is particularly evident in Fig. 8, which shows how the normalized TCD signal changes in a series of experiments conducted with hematite powder at different temperatures.

The experimental results highlight critical aspects of the reduction process. The shape and slope of the curves are clearly related to the rate at which the reducing agent is consumed, with a significantly increased rate at higher temperatures, but can also be influenced by the reaction equilibria. Comparative tests with different pure and commercial solid samples with the same methodology have also shown that the morphological and structural nature of the sample plays a key role and should be taken into consideration in the interpretation of the signals.

This suggests that changes in slope can also be attributed to changes in the solid surface area accessible to the gas and its evolution during the reaction [36,37]. Given the high sampling frequency of the TCD signal, the signal was down-sampled to 20 s between the points to improve the clarity of the data representation in the figures that follow.

3.2.1. Temperature effect

Temperature is one of the most significant variables in the study of iron oxide reduction. An increased temperature improves the kinetics and efficiency of the process but also affects the equilibrium conditions. In particular, operation above the eutectoid point in the Baur–Glassner

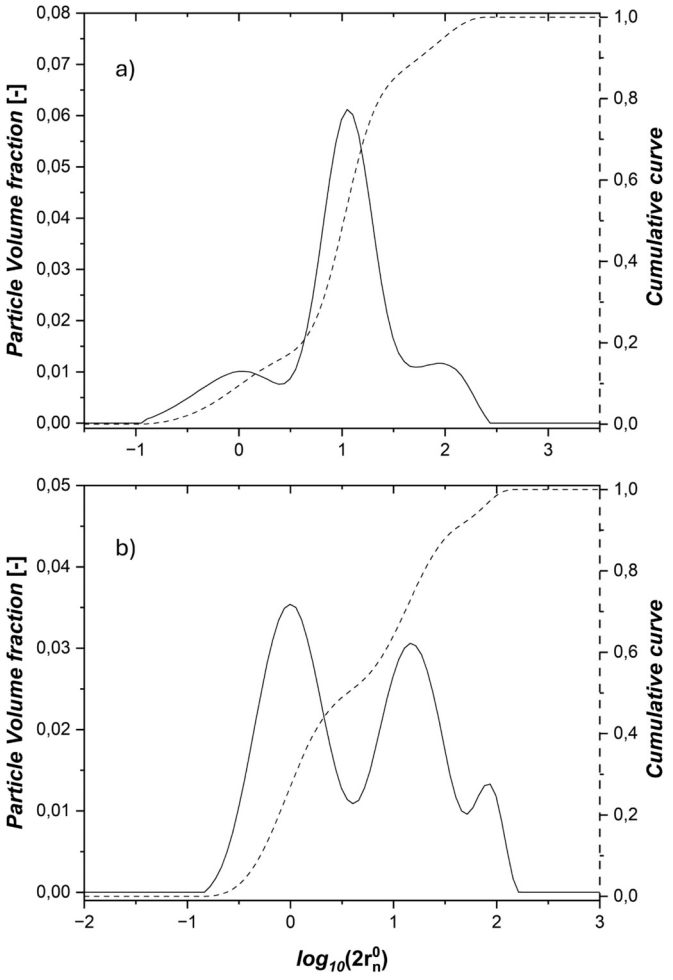

Fig. 7. Granulometric distribution of a) Fe_2O_3 Sigma A, and b) Fe_3O_4 Sigma A.

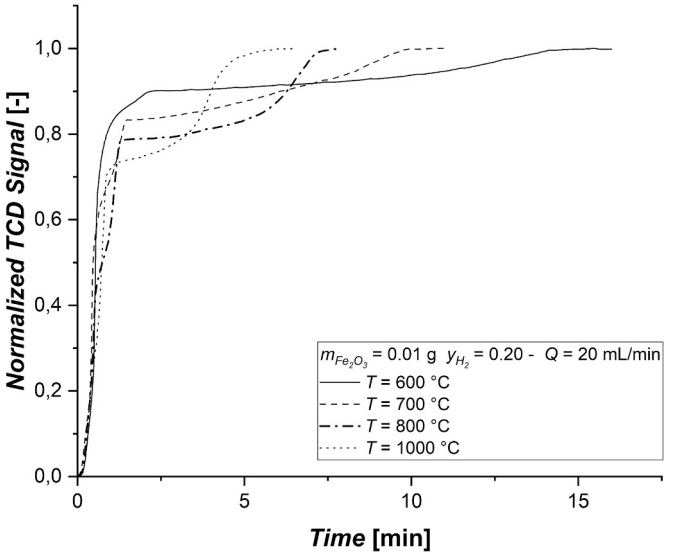

Fig. 8. Normalized TCD signal in Fe_2O_3 reduction experiments: $m_{Fe_2O_3} = 0.010$ g, $y_{H_2} = 0.20, Q = 20$ mL/min, $T = 600^{\circ}$C, 700°C, 800°C and 1000°C.

diagram (i.e., about 570 °C) allows access to the stability region for the sequential reduction reactions from Fe_3O_4 to FeO and from FeO to Fe. As temperature increases, thermodynamics increasingly favors these two

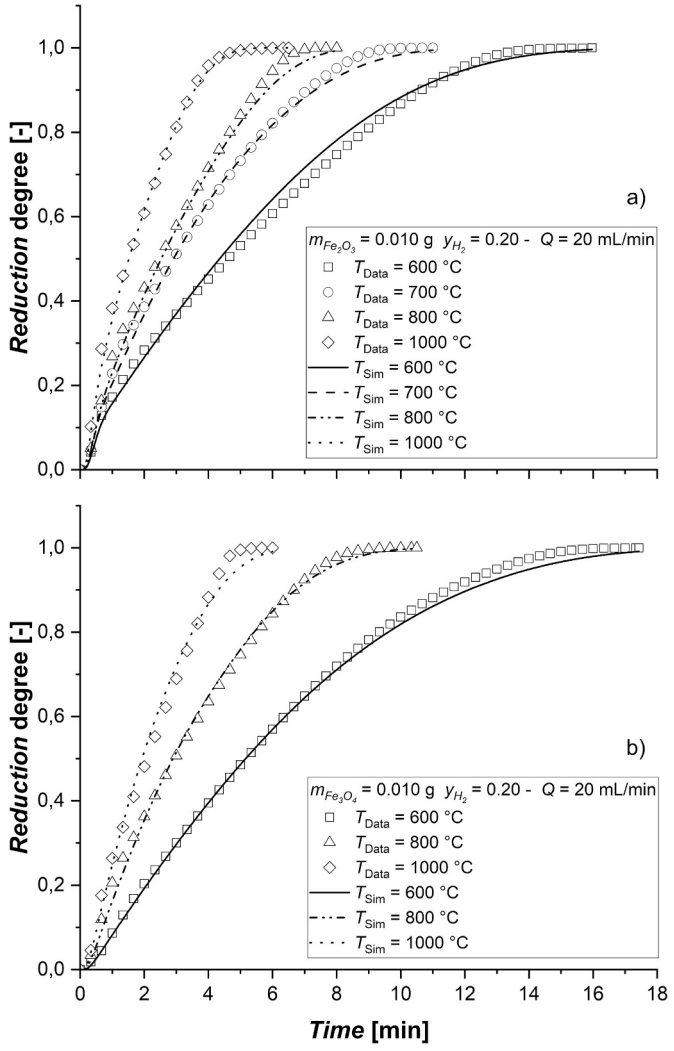

Fig. 9. Effect of temperature on a) Fe_2O_3 and b) Fe_3O_4 reduction under general experimental conditions: $m = 0.010$ g, $y_{H_2} = 0.20, Q = 20$ mL/min. Experimental results indicated by markers, simulated results by solid, dash-dotted and dotted lines.

reactions, significantly expanding the range of water vapor concentrations that do not inhibit the chemical process (Fig. 1). The markers in Fig. 9 show the effects of temperature on the overall degree of reduction of pure hematite and magnetite over time in the reduction experiments.

Comparing Figs. 8 and 9, which are different representations of the same experimental results, the differences between the normalized TCD signal become more pronounced through the integration procedure. In this way, important process characteristics become clear particularly in the early first part of the reaction. It is obvious that increasing the operating temperature significantly reduces the overall reduction time due to the increase in reaction rate and consequent hydrogen consumption. The results show that the complete conversion of hematite to magnetite takes place in less than one minute under all experimental conditions: a significant change in the slope can be observed at a degree of conversion of around 0.11. This value corresponds to the completion of the first reduction step, which is fast and thermodynamically unhindered. As for the reduction of Fe_3O_4 to FeO, the slope transitions in the thin-layer experiments are less pronounced than in the fixed-bed experiments (Fig. 6a). This is due to the small mass of solids used in the experiments: the water vapor produced is removed very efficiently, which supports not only the second but also the third reduction stage. For this reason, these reduction steps can occur almost simultaneously,

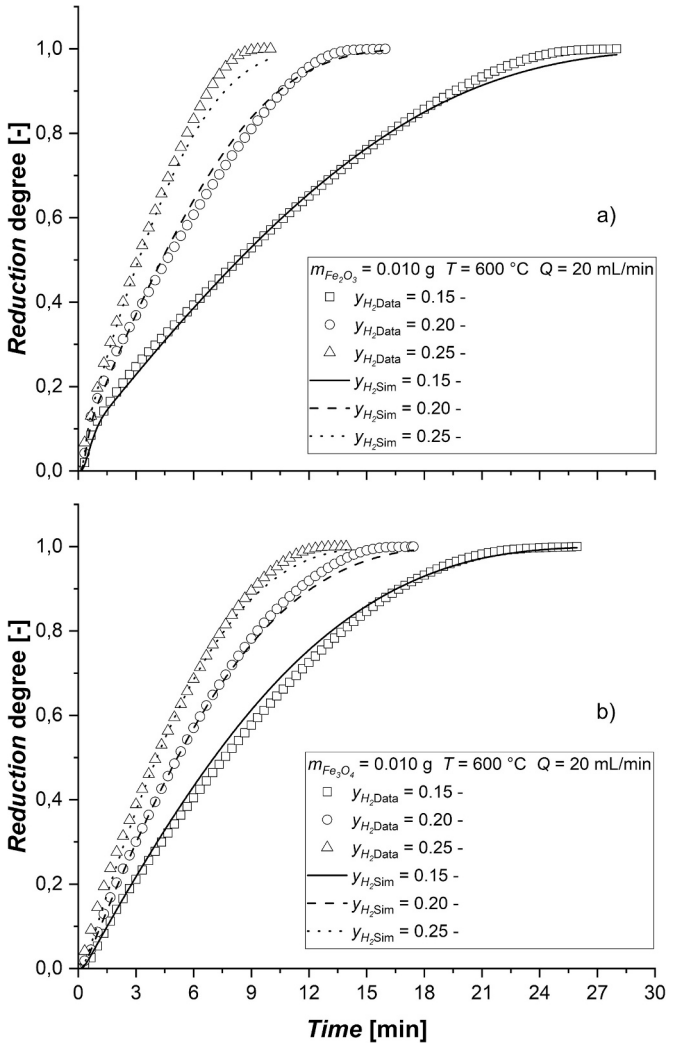

Fig. 10. Effect of feed gas hydrogen content on a) Fe_2O_3 and b) Fe_3O_4 reduction under general experimental conditions: m = 0.010 g, T = 600°C, Q = 20 mL/min. Experimental results indicated by markers, simulated results by solid, dash-dotted, and dotted lines.

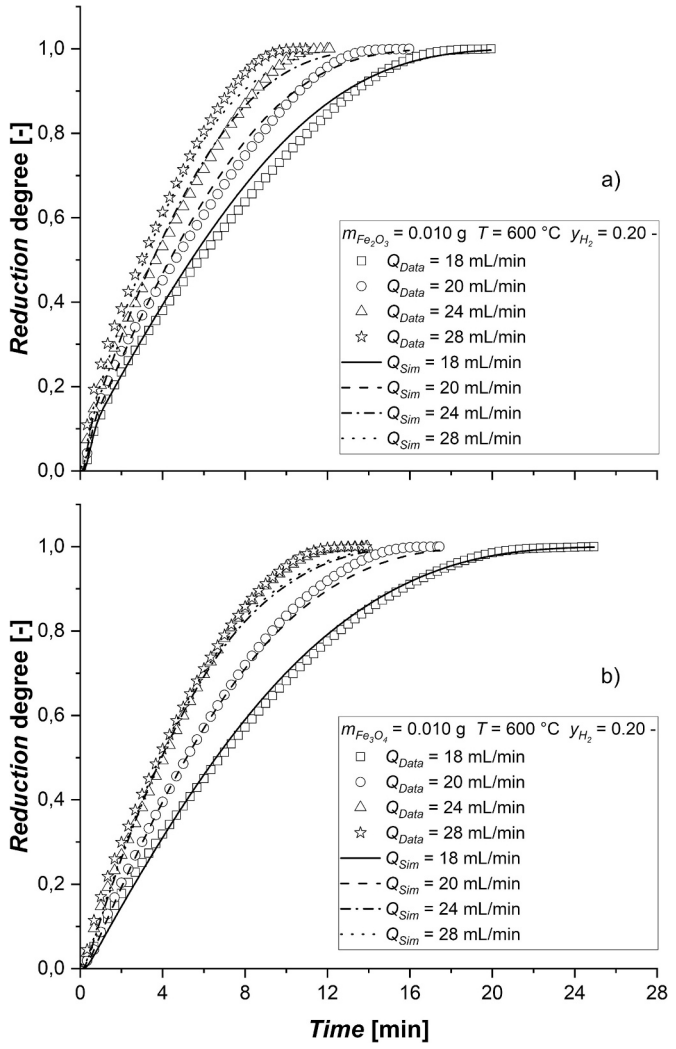

Fig. 11. Effect of volumetric flow of feed gas on a) Fe_2O_3 and b) Fe_3O_4 reduction under general experimental conditions: m = 0.010 g, T = 600°C, y_{H_2} = 0.20. Experimental results indicated by markers, simulated results by solid, dash-dotted, and dotted lines.

so it is difficult to distinguish between them. The reduction of magnetite cannot be considered completed at an overall conversion degree of about 0.3 as this likely includes a contribution from the FeO-to-Fe step. The final, slower step is clearly the reduction of wüstite, as widely reported in literature [15]. The differences in reduction rates between hematite and magnetite powders, especially at lower temperatures (e.g., 600 °C) are mainly due to the difference in particle size distribution, which slows down the reaction for the latter case. This gap is only closed at the highest temperatures.

3.2.2. *Effect of gas composition*

The effect of the composition of the feed gas was studied by changing molar fraction of the hydrogen (y_{H_2}), with the balance being inert gas (Ar), affecting the driving force of the reactions, with results for hematite and magnetite sample reported in Fig. 10.

As expected, an increased hydrogen content significantly decreases the overall time required to complete the reduction process. A high availability of hydrogen enhances the driving force and reaction rates in all steps. In addition, at higher H_2:Ar molar ratios, thermodynamic limitations are reduced or even removed. The reduction of Fe_2O_3 is consistently faster than that of Fe_3O_4, attributed theoretically to the crystal structure of Fe_3O_4, which has a stronger binding force for oxygen than Fe_2O_3. In this case, the much larger particle size distribution in the magnetite sample also slows down the reaction kinetics. A comparison between the two data sets shows that the effect of the operating parameters becomes less significant when large particles are present.

3.2.3. *Effect of volumetric gas flow rate*

Finally, the influence of the total volumetric flow rate (Q) of the feed gas was investigated. This variable significantly influences the convection phenomena within the reactor system (Eqs. (1) and (5)). An insufficient flow rate can lead to an excessive accumulation of water vapor in the bed, limiting the reaction progress due to thermodynamic constraints. Conversely, increasing the flow rate helps to maintain a high hydrogen concentration throughout the process, which promotes the progress of the reaction in all phases. Fig. 11 illustrates the effect of the gas flow rate on the reduction behavior of pure hematite and magnetite.

Increasing the flow rate clearly reduces the overall reduction time. For pure hematite, this variable appears to have the least impact, while for magnetite it has a greater effect. The experimental data reveals that the difference between 24 mL/min and 28 mL/min is minor for hematite and practically negligible for magnetite.

3.3. *Parameter estimation*

In the parametric analysis, the experimental trials were separated by

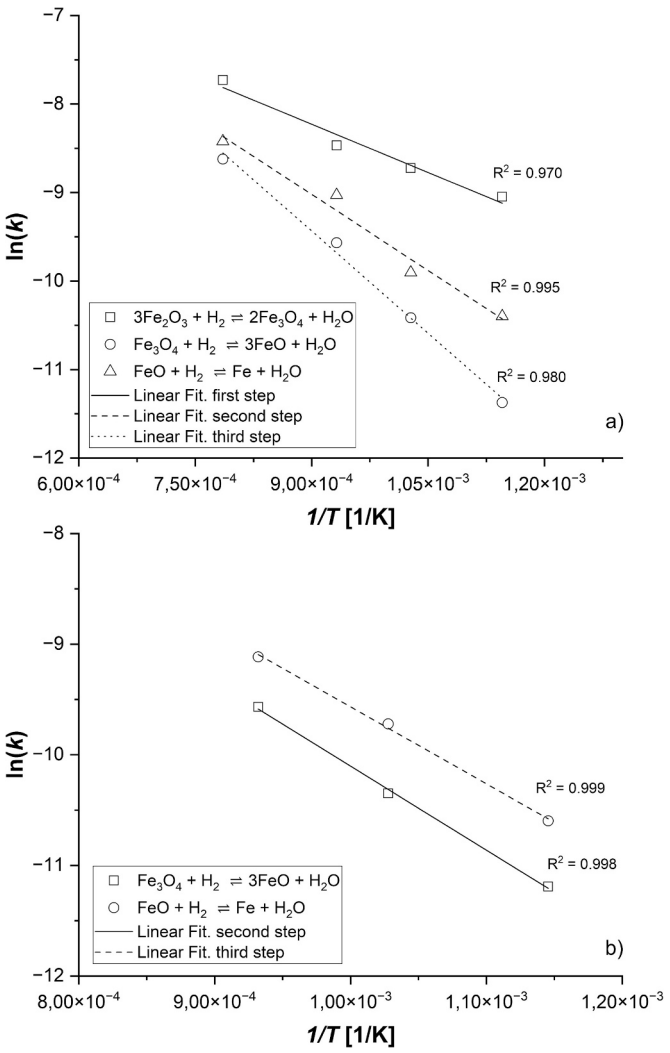

Fig. 12. Arrhenius plots for a) Fe_2O_3 and b) Fe_3O_4 reduction.

Table 3
Estimated parameters in the reaction rate expressions.

Starting material	Reactions	E_a	$k_{j,\mathrm{ref}}$	R^2
Fe_2O_3	$Fe_2O_3 \rightleftharpoons Fe_3O_4$	30 ± 4	$7 \bullet 10^{-3} \pm 6 \bullet 10^{-4}$	0.970
Fe_2O_3	$Fe_3O_4 \rightleftharpoons FeO$	64 ± 3	$8 \bullet 10^{-2} \pm 1 \bullet 10^{-2}$	0.995
Fe_2O_3	$FeO \rightleftharpoons Fe$	48 ± 5	$2 \bullet 10^{-2} \pm 3 \bullet 10^{-3}$	0.980
Fe_3O_4	$Fe_3O_4 \rightleftharpoons FeO$	64 ± 2	$8 \bullet 10^{-2} \pm 9 \bullet 10^{-3}$	0.999
Fe_3O_4	$FeO \rightleftharpoons Fe$	58 ± 3	$7 \bullet 10^{-2} \pm 9 \bullet 10^{-3}$	0.998

temperature and solid type. The kinetic parameters estimated in this study were determined through a simultaneous evaluation of the three reduction steps. The mathematical model developed here discretizes the solid phase and allows the coexistence of multiple reaction fronts within the same particle whenever dictated by local conditions. This formulation naturally accommodates the experimentally observed overlap of the reactions, rather than imposing strictly sequential progression. At each reaction instant, the model calculates the degrees of reduction associated with each elementary step, whose sum yields the overall degree of reduction (Eq. (26)), directly comparable to the experimental data. With this approach, the contributions of the individual reactions to the global rate enable the evaluation of distinct kinetic constants.

For each set of experimental data, the kinetic constants k_j were evaluated with respect to the available reactions. Using the linearized Arrhenius equation, the natural logarithm of the constants was plotted against the reciprocal of the temperature. For hematite as starting material, this approach yielded four data points for each of the three reactions and for magnetite, three points for each of the two reactions. Fig. 12 shows the resulting Arrhenius plots, while Table 3 contains the calculated activation energies and reference kinetic constants together with the respective errors from the linear regression.

The Arrhenius plots in Fig. 12 show a clear and consistent trend in the calculated values of k_j. This result is supported by the low errors observed when estimating the activation energies and pre-exponential factors using the linearized Arrhenius equation. In particular, the errors for $E_{a,j}$ fall below 11% and for k_j below 15%. As far as the first reduction step is concerned, the reaction always proceeds very quickly, especially at higher temperatures. For this reason, the use of a high-precision, high-frequency measuring device was crucial. As can be seen for all the experiments, the mathematical model successfully reproduces observed conversion, as seen by the agreement between the continuous lines and the markers in Figures from 9 to 11. This can be observed especially in the case study on the temperature effect (c.f. Fig. 9). This shows that there are no significant morphological and structural changes in the solid due to temperature, especially in terms of porosity (surface area) and granulometric distribution conditions defined by the characterization techniques. One notable exception in the description of experimental data is in the gas composition effect result during the last phase of the hematite reduction where the hydrogen fraction is about 0.15 (c.f. Fig. 10). This deviation may be explained by a possible error in the small mass (10 mg) of the sample: a weighing error to the fourth decimal place could cause such a discrepancy, especially in the slower final phase of the reduction [66]. Finally, the simulation results related to the volumetric flow rate effect show excellent agreement with the experimental data at higher flow rates, while at lower flow rates a slight underestimation of the final reduction degree can be observed.

4. Discussion

Many kinetic models have been proposed for the hydrogen-based reduction of iron oxides. These models generally fall into two broad categories: phenomenological models (like Avrami-type formulations) and physicochemical models. The latter includes comprehensive approaches such as the Random Pore Model and Grain Model, which are specifically designed to capture the structural evolution and diffusion limitations occurring within the solid during reduction [60].

Models like the RPM and GM are particularly suited for analyzing the reduction kinetics of pellets or larger agglomerates, where the internal structure (porosity, tortuosity) significantly evolves and mass-transfer resistances can become dominant. Several studies show that the internal structure and solid organization can change drastically with the operating condition such as temperature [29,39] or, in the case of H_2-based reduction, the presence of water vapor [71,72]. In stark contrast, the present study employs an experimental configuration using thin beds of pure oxide powders, intentionally designed to minimize mass-transfer effects. This methodological choice allows for the extraction of kinetic parameters that closely reflect the intrinsic chemical reactivity of the system, without the need for complex structural assumptions (e.g., pore distribution) inherent to models like the RPM or GM. The proposed Shrinking Core Model is an appropriate choice for isolating this intrinsic chemical step under our controlled conditions. The reliability of this approach is confirmed by the resulting activation energies: 74.8 ± 49.0 kJ mol^{-1} for hematite reduction, 66.0 ± 57.2 kJ mol^{-1} for magnetite reduction, and 62.0 ± 43.9 kJ mol^{-1} for the final step [60]. These values fall within the statistically expected literature ranges. The SCM, validated here, can nevertheless be extended to a grain-level or multiscale description if future analyses of commercial materials warrant the incorporation of structural factors.

The results have clearly shown that the mathematical model is capable of accurately describing the experimental data on the reduction

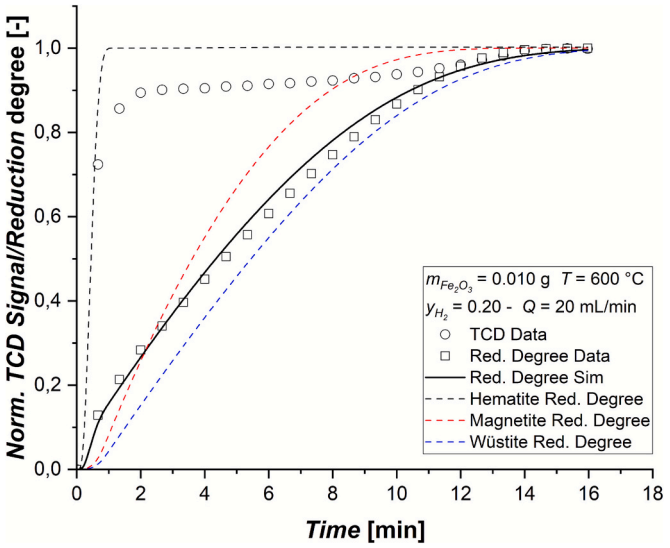

Fig. 13. Experimental and simulation results of reduction of thin layers of hematite under the experimental conditions $m_{Fe_2O_3} = 0.010\,g$, $T = 600^{\circ}C$, $y_{H_2} = 0.20$, $Q = 20\,mL/min$.

of hematite and magnetite in hydrogen-containing gas flows. However, in order to achieve a better understanding of the reduction process, it is necessary to utilize the simulation to its full capacity. This approach is essential not only to gain insight into key aspects of the system under investigation, but also to assess the quality and consistency of the results with theoretical model assumptions and as a comparison with data reported in the literature. Fig. 13 presents the evolution of the individual reduction degrees X_j for each solid species and the progress of the overall reduction reaction for a thin solid layer experiment. These average values are used because even in a mathematically discretized thin bed, slight variations in the reduction dynamics occur. In particular, the simulated average overall reduction degree ($\overline{X}$) — as described in the section on the numerical solution — is used to fit the experimental data. An important finding from Fig. 13 is that the reaction fronts of the different steps never overlap during the whole process. This important aspect is often neglected in modeling studies of iron oxide reduction but is crucial in heterogeneous non-catalytic reactions in the specific case of reactions in series: the conversion from one solid species to the next is not directly coupled in the mass balances, which requires careful mathematical control and validation of the adjustment of the kinetic parameters by simulation tests.

The standard test case shown (i.e., test H2) confirms that hematite is rapidly converted within the first minute under the given conditions, with minimal overlap with the subsequent reduction step. For the later steps, where the magnetite and wüstite reduction have closely following reaction fronts, a separate evaluation cannot be adopted. This can be explained by the fact that the driving force in thin iron oxide layers remains very high due to a low accumulation of water vapor. Although the reactions proceed quickly with a maximum of H_2O formation in the hematite step and the larger amount of H_2O formation in the following steps, the low height of the solid layer prevents hydrogen starvation and an accumulation of oxidizing agents. Further information provided in Fig. S6 (Supplementary Materials) shows simulation results in the form of contour plots of the dynamic evolution of solid and gas composition over time in the thin film fixed bed. Since there are practically no thermodynamic limitations — especially for FeO — the reactions can take place simultaneously and the reduction can be completed within minutes. The small amount of reducing agent and the limited flow rate were deliberately chosen in the experimental design to prevent excessively fast reactions to allow for adequate observation of the reduction dynamics. In the latter case, thermodynamics plays a pivotal role in governing the reaction fronts. As is also shown, the evolution of the average overall reduction degree — calculated starting from the sum of the reduction degrees across all particle size classes — starts increasing with a slight delay, which is mainly due to the initial dilution of the reducing gas in the inert carrier. A significant change in the slope only occurs when the hematite reduction has been completed. The second phase is much more uniform due to the overlap of the subsequent reactions, which prevents the occurrence of a clearly dominant solid phase species responsible for hydrogen consumption. Based on these considerations, all simulations associated with the experimental data were thoroughly checked after parameter fitting to evaluate the quality of the results.

Regarding regime control, it is generally assumed that if half of the calculated activation energy is just below or equal to 20 kJ mol^{-1}, there is a mixture of internal diffusion and chemical control. From a numerical point of view, the comparison of the activation energies and the pre-exponential factors for the second reduction step shows almost identical values. This finding is consistent with the results presented in Fig. 13, which show that hematite reduction is almost completely independent of magnetite reduction in terms of hydrogen consumption. This separation of the contributions allows for a reliable estimation of the kinetic parameters for the second reaction step. In both cases, the activation energy values suggest that the controlling regime is chemical.

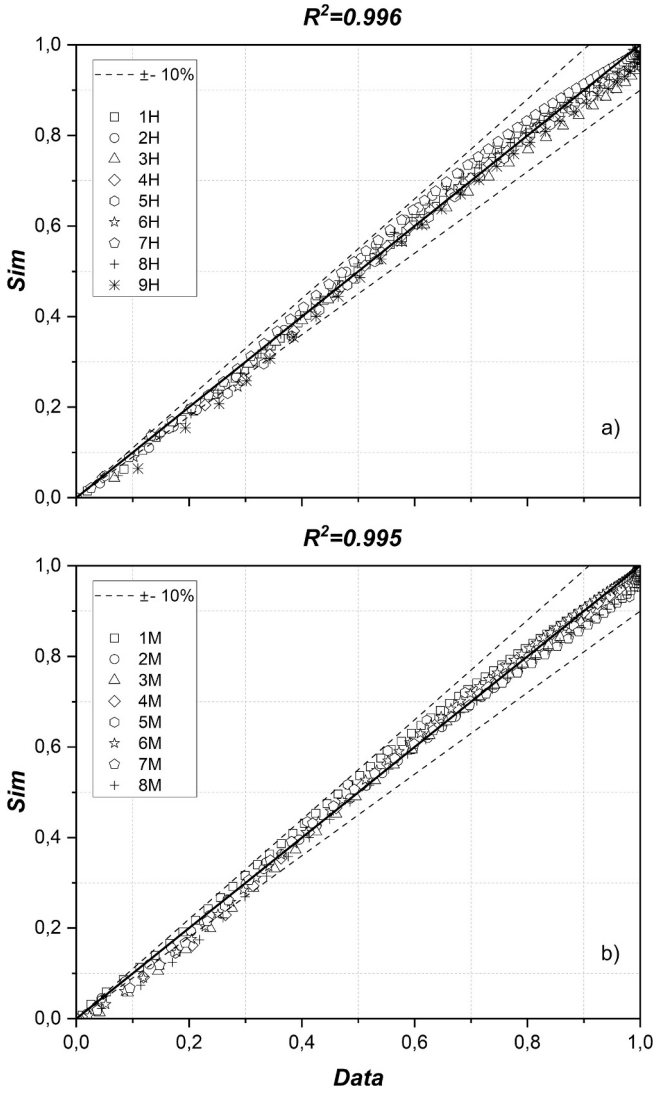

Fig. 14. Reduction degree parity plots: Experiments vs. simulations of a) Fe_2O_3 and b) Fe_3O_4 reduction in hydrogen-containing gas.

The third and final step shows slightly different activation energies for the two solids, but the controlling regime remains chemical in both cases. The discrepancies can be attributed to differences in particle size distribution. In particular, the last step of the reduction, where more water vapor is produced, is sensitive to the particle radius as an operating parameter [66]. It is interesting to compare the results obtained in this study with the values reported in the literature. The calculated activation energies are within the reported ranges but also agree well with the average values defined for each specific reaction step [60]. The wide variability in kinetic parameters reported in the literature is largely due to differences in solid sample history, purity, intrinsic properties, and post-synthesis treatments. In addition, many modeling approaches are based on simplified assumptions and kinetic parameters that often reflect apparent rather than intrinsic activation energies.

The choice of a rigorous experimental approach coupled with the use of a flexible mathematical model based on solid-phase approximations that reflect the experimental observations of intrinsic properties has thus led to consistent results, resulting in kinetic parameters in the model that successfully describes all experimental data for both data sets. A summary of the agreement between simulations and experiments is provided in the double parity plot of the reduction degrees in Fig. 14. As can be seen from the plots the comparison between experimental and simulated data, down-sampled to 30 s between the points, is largely within a variability of ±10%. The goodness of fit is confirmed by the coefficients of determination, with $R^2 = 0.996$ for the reduction of pure hematite and $R^2 = 0.995$ for the reduction of pure magnetite and by the low root mean square errors, which are RMSE = 0.021 and RMSE = 0.020, respectively.

5. Conclusions

In this work, a comprehensive experimental and modeling investigation of a system for the reduction of thin beds of iron oxide fines with hydrogen as a reducing agent was presented. The experiments were conducted in a packed bed reactor-like system under different operating conditions, including temperature, hydrogen content, total volumetric flow rate and oxide type. Two pure powdered oxides — hematite and magnetite — were used. The experimental campaigns allowed for a detailed analysis of the reduction kinetics in the different reaction steps facilitated by an accurate analysis method based on measurements of the thermal conductivity of the outlet gas. Through rigorous mathematical data processing, the experimental signal was successfully correlated with the degree of conversion of the solid reactant. This innovative approach was further validated by combining the results of chemical and granulometric analyses of the solids with the consistent results of the developed mathematical model. A dynamic model of the shrinking core with multiple interfaces was coupled with a classical axial dispersion model to account for both particle and reactor phenomena, including gas-phase transport through the empty reactor space and the solid bed. The model was able to accurately reproduce the new experimental data. Based on a large data set of systematic reduction experiments performed under different conditions, the kinetic parameters for each individual reaction step were rigorously determined and compared with values reported in the literature. This enabled a thorough and comprehensive evaluation of the entire reduction process. An important finding of the work is the small influence of thermodynamic constraints on the reduction process, which is due to the negligible residence time of the locally generated water vapor in the solid phase in the present setup. This leads to a strong driving force of the reducing gas. The reduction of hematite to magnetite is extremely rapid and is governed by a mixture of internal diffusion and chemical regime. The subsequent reductions of magnetite and wüstite are similarly rapid and are both governed by chemical control, although a slight difference in activation energy was observed in the third reduction step depending on the type of sample (hematite vs. magnetite) used. Using micron-scale powders and thin fixed beds made it possible to determinate the intrinsic kinetics of hydrogen reduction of iron oxides under conditions that minimize internal and external transport limitations. The kinetic parameters obtained were further validated in another study, which investigated a broader set of reduction experiments on packed beds of hematite powders, analyzing in more detail the role of emerging phenomena, including the influence of water vapor on thermodynamics and kinetics. This methodological roadmap includes extending the experiments to commercial fines obtained from BF and DRI pellets to evaluate the influence of morphology and chemistry, with dedicated structural evolution based on detailed characterization. The final step will be scaling up to full-size pellets through more complex modeling approaches (e.g., GM), integrating the phenomena and the resulting kinetic expressions into reactor-scale simulations. Generally, these results provide a valuable starting point for the evaluation of increasingly complex reduction systems, both experimentally and from a modeling perspective helping the development of future hydrogen-based technologies aimed at reducing the carbon footprint of the ironmaking sector.

Notation

Abbreviations

BF	Blast Furnace
CFD	Computational Fluid Dynamic
GM	Grain model
GOD	Gas Oxidant Degree
DRI	Direct Reduction Iron
LS	Light scattering
RMSE	Root mean square errors
RPM	Random pore model
SCM	Shrinking core model
TCD	Thermal conductivity detector

Symbols

A_j	Kinetic reaction resistance [s/m]
a_j	Proportional oxygen content parameter [−]
B_j	Intraparticle diffusion resistance [s/m]
c_i	Concentration *i:*th gas in the reactor [mol/m^3]
$c_{i,\text{in}}$	Feed *i:*th gas concentration [mol/m^3]
D_j	Intraparticle diffusion coefficient *j:*th reaction front [m^2/s]
D_{mol}	Molecular diffusivity coefficient [m^2/s]
D_z	Axial dispersion coefficient [m^2/s]
$d_{1,j}$	First coefficient empirical interparticle diffusion equation [m^2/s]
$d_{2,j}$	Second coefficient empirical interparticle diffusion equation [−]
$d_{3,j}$	Third coefficient empirical interparticle diffusion equation [K]
$E_{a,j}$	Activation energy *j:*th reaction front [J/mol]
e	Fitting parameter error
F	External diffusion resistance [s/m]
$g_{1,i}$	First coefficient in empirical thermal conductivity equation [W/(m K)]
$g_{2,i}$	Second coefficient in empirical thermal conductivity equation [−]
$g_{3,i}$	Third coefficient in empirical thermal conductivity equation [−]
$g_{4,i}$	Fourth coefficient in empirical thermal conductivity [−]
H	External diffusion coefficient [m/s]
h	Height of the solid bed [m]
K_j	Equilibrium constant *j:*th reaction front [−]
k_j	Kinetic constant *j:*th reaction front [m/s]
$k_{j,\text{ref}}$	Pre-exponential kinetic factor *j:*th reaction front [m/s]
L	Reactor length [m]
M	Molecular weight [g/mol]

m	Iron oxide initial mass [g]
$m_{1,i}$	First coefficient in empirical viscosity equation [Pa s]
$m_{2,i}$	Second coefficient in empirical viscosity equation [−]
$m_{3,i}$	Third coefficient in empirical viscosity equation [−]
$m_{4,i}$	Fourth coefficient in empirical viscosity equation [−]
N	Number of granulometric families [−]
N_j	Effective reaction SCM term ($f = 1$ [−], $f = 2$ [s^2/m^2], $f = 3$ [s^3/m^3])
n_0	Initial concentration of oxygen [mol/m^3]
O	Objective function
P	Operating pressure [N/m^2]
Pe	Pcclet number [−]
Q	Volume flow rate [mL/min]
R	Reactor radius [m]
R_g	Ideal gas constant [J/(K mol)]
Re	Reynolds number [−]
r_n^0	Iron oxide particle radius [m]
r_j	Reduction rate SCM [$mol/(m^3\ s)$]
S	Reactor cross sectional area [m^2]
Sc	Schmidt number [−]
Sh	Sherwood number [−]
T	Operating temperature [K]
t	Time [s]
u	Gas velocity [m/s]
V	Solid volume [m^3]
v_i	Diffusion volumes coefficients [−]
W	Total resistance ($f = 1$ [−]) ($f = 2$ [s^2/m^2]) ($f = 3$ [s^3/m^3])
X_j	Reduction degree *j:*th reaction front [−]
x_n	Weight granulometric distribution [−]
$y_{i,j}$	Gas molar fraction *i:*th species of *j:*th reaction front [−]
$y_{H_2,j,eq}$	Equilibrium molar fraction of H_2 of *j:*th reaction front [−]
z	Reactor axial coordinate [−]
β	Unit conversion term [$(m^3/min)/(dm^3/s)$]
ΔG_j	Gibbs free energy changes *j:*th reaction front [J/mol]
ΔH_j	Enthalpy changes *j:*th reaction front [J/mol]
ΔS_j	Entropy changes *j:*th reaction front [J/mol]
Δt	Maximum integration step
ε	Bed void degree [−]
λ_j	Solid thermal conductivity [W/(m K)]
ρ	Solid density [g/cm^3]
ρ_g	Gas density [g/cm^3]
$\nu_{i,j}$	Stoichiometric matrix [−]
μ_g	Gas viscosity [Pa s]

Subscripts

f	Number of available reaction fronts
i	Gas species
j	Reaction fronts
l	Spatial reactor domain
n	Index of granulometric family's distribution
s	Index of signal data distribution

Superscripts

0	index of initial condition [−]

CRediT authorship contribution statement

Emiliano Salucci: Writing – review & editing, Writing – original draft, Validation, Software, Methodology, Formal analysis, Data curation. **Antonio D'Angelo:** Methodology, Investigation, Data curation. **Vincenzo Russo:** Writing – review & editing, Conceptualization. **Henrik Grénman:** Writing – review & editing, Project administration, Conceptualization. **Henrik Saxén:** Writing – review & editing, Project administration, Methodology, Funding acquisition, Conceptualization.

Declaration of competing interest

The authors declare that they have no known competing financial interests or personal relationships that could have appeared to influence the work reported in this paper.

Acknowledgements

We gratefully acknowledge financial support from the European Union within the projects *Minimisation of CO_2 Emissions from the BF by hydrogen containing injectants and use of DRI/HBI during transition to new Ironmaking processes until 2030* (grant agreement 101057790) and *Maximise H_2 Enrichment in Direct Reduction Shaft Furnaces* (grant agreement 101058429). Views and opinions expressed in the paper are, however, those of the authors only and do not necessarily reflect those of the European Union: neither the European Union nor the other granting authority can be held responsible for them.

Funded by the European Union

Appendix A. Supplementary data

Supplementary data to this article can be found online at https://doi.org/10.1016/j.cej.2026.172848.

Data availability

Data will be made available on request.

References

[1] M. Geerdes, et al., Modern Blast Furnace Ironmaking an Introduction, 2020, https://doi.org/10.3233/STAL9781643681238.
[2] worldsteel association, 2024 World Steel in Figures, Accessed: Apr. 14, 2025. [Online]. Available: https://worldsteel.org/wp-content/uploads/World-Steel-in-Figures-2024.pdf, 2024.
[3] U.S. Energy Information Administration, Industrial Sector Energy Consumption, Accessed: Jul. 07, 2024. [Online]. Available: https://www.iea.org/energy-system/industry, 2016.
[4] M.A. Quader, S. Ahmed, R.A.R. Ghazilla, S. Ahmed, M. Dahari, A Comprehensive Review on Energy Efficient CO2 Breakthrough Technologies for Sustainable Green Iron and Steel Manufacturing, Elsevier Ltd, May 30, 2015, https://doi.org/10.1016/j.rser.2015.05.026.
[5] H. Kildahl, L. Wang, L. Tong, Y. Ding, Cost effective decarbonisation of blast furnace – basic oxygen furnace steel production through thermochemical sector coupling, J. Clean. Prod. 389 (Feb. 2023) 135963, https://doi.org/10.1016/j.jclepro.2023.135963.
[6] J.G. Peacey, W.G. Davenport, The Iron Blast Furnace, Elsevier, 1979, https://doi.org/10.1016/C2013-0-03066-6.
[7] W.P. Hutny, G.K. Lee, J.T. Price, Fundamentals of coal combustion during injection into a blast furnace, Prog. Energy Combust. Sci. 17 (4) (Jan. 1991) 373–395, https://doi.org/10.1016/0360-1285(91)90008-B.
[8] C.W. Bale, et al., FactSage Thermochemical Software and Databases - 2010 - 2016, Calphad, 2016. www.factsage.com.
[9] J. Moon, V. Sahajwalla, Investigation into the role of the boudouard reaction in self-reducing iron oxide and carbon briquettes, Metall. Mater. Trans. B 37 (2) (Apr. 2006) 215–221, https://doi.org/10.1007/BF02693151.
[10] Y. Pan, H. Zuo, J. Wang, Q. Xue, G. Wang, X. She, Review on improving gas permeability of blast furnace, J. Iron Steel Res. Int. 27 (2) (Feb. 2020) 121–131, https://doi.org/10.1007/s42243-019-00321-y.
[11] L.F. Verdeja González, D. Fernández González, J.I. Verdeja González, The Basic Oxygen Furnace to Obtain Steel, 2021, pp. 1–81, https://doi.org/10.1007/978-3-030-68000-8_1.
[12] M. Atsushi, H. Uemura, T. Sakaguchi, MIDREX Process, Accessed: Nov. 23, 2023. [Online]. Available: https://www.kobelco.co.jp/english/ktr/pdf/ktr_29/050-057.pdf, 2010.
[13] M. Kirschen, K. Badr, H. Pfeifer, Influence of direct reduced iron on the energy balance of the electric arc furnace in steel industry, Energy 36 (10) (Oct. 2011) 6146–6155, https://doi.org/10.1016/j.energy.2011.07.050.

[14] P. Cavaliere, Direct reduced iron: most efficient technologies for greenhouse emissions abatement, in: Clean Ironmaking and Steelmaking Processes, Springer International Publishing, 2019, pp. 419–484, https://doi.org/10.1007/978-3-030-21209-4_8.

[15] D. Spreitzer, J. Schenk, Reduction of Iron Oxides with Hydrogen—A Review, Wiley-VCH Verlag, Oct. 01, 2019, https://doi.org/10.1002/srin.201900108.

[16] C.J.M. Hessels, T.A.M. Homan, N.G. Deen, Y. Tang, Reduction kinetics of combusted iron powder using hydrogen, Powder Technol. 407 (Jul. 2022), https://doi.org/10.1016/j.powtec.2022.117540.

[17] P. Garg, X. Hu, Y. Li, K. Li, S. Nag, J. Zhang, Kinetics of Iron oxide reduction in H 2/H 2O gas mixture: global and stepwise reduction, Metall. Mater. Trans. B Process Metall. Mater. Process. Sci. 53 (3) (Jun. 2022) 1759–1774, https://doi.org/10.1007/s11663-022-02485-7.

[18] Q. Tang, K. Huang, Determining the kinetic rate constants of Fe3O4-to-Fe and FeO-to-Fe reduction by H2, Chem. Eng. J. 434 (Apr. 2022), https://doi.org/10.1016/j.cej.2022.134771.

[19] K. He, Z. Zheng, Z. Chen, H. Chen, W. Hao, Kinetics of hydrogen reduction of Brazilian hematite in a micro-fluidized bed, Int. J. Hydrog. Energy 46 (5) (Jan. 2021) 4592–4605, https://doi.org/10.1016/j.ijhydene.2020.10.263.

[20] A.H.A. El-Geassy, Rate controlling step in the reduction of iron oxides; kinetics and mechanism of wüstite-iron step in H2, CO and H2/CO gas mixtures, in: IOP Conference Series: Materials Science and Engineering, Institute of Physics Publishing, Sep. 2017, https://doi.org/10.1088/1757-899X/229/1/012002.

[21] M.L. Ali, Q. Fradet, U. Riedel, Particle-resolved computational modeling of hydrogen-based direct reduction of iron ore pellets in a fixed bed. Part I: methodology and validation, Int. J. Hydrog. Energy 87 (Oct. 2024) 332–343, https://doi.org/10.1016/j.ijhydene.2024.09.028.

[22] S. Liu, Q. Zhang, Thermodynamic calculation on the reduction of iron oxide in an H2 atmosphere, Int. J. Thermodyn. 10 (3) (2007) 113–119.

[23] W. Zhang, et al., Thermodynamic analyses of Iron oxides redox reactions, in: Proceedings of the 8th Pacific Rim International Congress on Advanced Materials and Processing, Springer International Publishing, Cham, 2013, pp. 777–789, https://doi.org/10.1007/978-3-319-48764-9_96.

[24] Y. Qu, Y. Yang, Z. Zou, C. Zeilstra, K. Meijer, R. Boom, Reduction kinetics of fine hematite ore particles with a high temperature drop tube furnace, ISIJ Int. 55 (5) (2015) 952–960, https://doi.org/10.2355/isijinternational.55.952.

[25] D.Q. Fan, H.Y. Sohn, M. Elzohiery, Analysis of the reduction rate of hematite concentrate particles in the solid state by H2 or CO in a drop-tube reactor through CFD modeling, Metall. Mater. Trans. B Process Metall. Mater. Process. Sci. 48 (5) (Oct. 2017) 2677–2684, https://doi.org/10.1007/s11663-017-1053-2.

[26] A.A. El-Geassy, M.I. Nasr, M.M. Hessien, Effect of reducing gas on the volume change during reduction of Iron oxide compacts, ISIJ Int. 36 (6) (1996) 640–649, https://doi.org/10.2355/isijinternational.36.640.

[27] M. Bernasowski, Theoretical study of the hydrogen influence on iron oxides reduction at the blast furnace process, Steel Res. Int. 85 (4) (Apr. 2014) 670–678, https://doi.org/10.1002/srin.201300141.

[28] A.A. El-Geassy, M.I. Nasr, Influence of the original structure on the kinetics of hydrogen reduction of hematite compacts, Trans. Iron Steel Inst. Japan 28 (8) (1988) 650–658, https://doi.org/10.2355/isijinternational1966.28.650.

[29] B. Sadeghi, P. Cavaliere, M. Bayat, N. Ebrahimzadeh Esfahani, A. Laska, D. Koszelow, Experimental study and numerical simulation on porosity dependent direct reducibility of high-grade iron oxide pellets in hydrogen, Int. J. Hydrog. Energy 69 (Jun. 2024) 586–607, https://doi.org/10.1016/j.ijhydene.2024.05.050.

[30] B. Hou, H. Zhang, H. Li, Q. Zhu, Study on kinetics of iron oxide reduction by hydrogen, Chin. J. Chem. Eng. 20 (1) (Feb. 2012) 10–17, https://doi.org/10.1016/S1004-9541(12)60357-7.

[31] A. Bonalde, A. Henriquez, M. Manrique, Kinetic Analysis of the Iron Oxide Reduction Using Hydrogen–Carbon Monoxide Mixtures as Reducing Agent vol. 45, no. 9, ISIJ International, 2005, pp. 1255–1260, https://doi.org/10.2355/isijinternational.45.1255.

[32] A.A. El-Geassy, V. Rajakumar, Influence of particle size on the gaseous reduction of wustite at 900-1100.DEG.C, Trans. Iron Steel Inst. Japan 25 (12) (1985) 1202–1211, https://doi.org/10.2355/isijinternational1966.25.1202.

[33] M.M. Khader, B.E. El-Anadouli, E. El-Nagar, B.G. Ateya, Kinetics of the reduction of Fe2O3 with hydrogen, J. Solid State Chem. 93 (2) (Aug. 1991) 283–290, https://doi.org/10.1016/0022-4596(91)90302-X.

[34] A. Hammam, et al., Isothermal and non-isothermal reduction behaviors of Iron ore compacts in pure hydrogen atmosphere and kinetic analysis, Min. Metall. Explor. 38 (1) (Feb. 2021) 81–93, https://doi.org/10.1007/s42461-020-00317-3.

[35] R.J. Longbottom, L. Kolbeinsen, Iron Ore Reduction with CO and H2 Gas Mixtures – Thermodynamic and Kinetic Modelling, Wollongong. Accessed: Jul. 01, 2024. [Online]. Available: https://ro.uow.edu.au/engpapers/1260/, Jan. 2008.

[36] A. D'Angelo, E. Salucci, V. Russo, H. Grenman, H. Saxén, Reduction Kinetics of Pure and Industrial Hematite Samples with Hydrogen in a Small Fixed Bed System, 2025, https://doi.org/10.2139/ssrn.5104362.

[37] A. D'Angelo, E. Salucci, V. Russo, H. Grénman, H. Saxén, Hydrogen reduction of Iron oxide powder in thin layers, Ind. Eng. Chem. Res. 64 (1) (Jan. 2025) 158–170, https://doi.org/10.1021/acs.iecr.4c03138.

[38] B. Sadeghi, et al., Reducibility of high-grade pellets directly reduced in hydrogen atmosphere: modeling and experimental procedure, Int. J. Hydrog. Energy 144 (Jul. 2025) 69–84, https://doi.org/10.1016/j.ijhydene.2025.06.020.

[39] P. Cavaliere, B. Sadeghi, L. Dijon, A. Laska, D. Koszelow, Three-dimensional characterization of porosity in iron ore pellets: a comprehensive study, Miner. Eng. 213 (Aug. 2024) 108746, https://doi.org/10.1016/j.mineng.2024.108746.

[40] N. Shigematsu, H. Iwai, Effect of CaO added with SiO2 and/or Al2O3 on reduction rate of dense wustite by hydrogen, ISIJ Int. 29 (6) (1989) 486–494, https://doi.org/10.2355/isijinternational.29.486.

[41] B. Sadeghi, M. Najafizadeh, P. Cavaliere, A. Shabani, M. Aminaei, Effect of composition and processing conditions on the direct reduction of iron oxide pellets, Powder Technol. 444 (Aug. 2024) 120061, https://doi.org/10.1016/j.powtec.2024.120061.

[42] S.S. Jung, J.S. Lee, In-situ kinetic study of hydrogen reduction of Fe2O3 for the production of Fe nanopowder, Mater. Trans. 50 (9) (Sep. 2009) 2270–2276, https://doi.org/10.2320/matertrans.MRA2008472.

[43] Z. Wei, et al., Reduction kinetics of hematite ore fines with H2 in a rotary drum reactor, Powder Technol. 332 (Jun. 2018) 18–26, https://doi.org/10.1016/j.powtec.2018.03.054.

[44] R. Takahashi, J. Yagi, Y. Omori, Reduction rate of iron oxide pellets with hydrogen, Phys. Chem. Metals (1971) 9–30. Accessed: Jul. 07, 2024. [Online]. Available: https://tohoku.repo.nii.ac.jp/record/46094/files/KJ00004197776.pdf.

[45] A. Kemppainen, O. Mattila, E.P. Heikkinen, T. Paananen, T. Fabritius, Effect of H2-H2O on the reduction of olivine pellets in CO-CO2 gas, ISIJ Int. 52 (11) (2012) 1973–1978, https://doi.org/10.2355/isijinternational.52.1973.

[46] G. Nabi, W.-K. Lu, The kinetics of hematite to magnetite reduction in hydrogen-water and hydrogen-water-nitrogen mixtures, Ind. Eng. Chem. Fundam. 13 (4) (Nov. 1974) 311–316, https://doi.org/10.1021/i160052a003.

[47] P. Rajput, B. Bhoi, S. Sahoo, R.K. Paramguru, B.K. Mishra, Preliminary investigation into direct reduction of iron in low temperature hydrogen plasma, Ironmak. Steelmak. 40 (1) (Jan. 2013) 61–68, https://doi.org/10.1179/1743281212Y.0000000023.

[48] A.A. Barde, J.F. Klausner, R. Mei, Solid state reaction kinetics of iron oxide reduction using hydrogen as a reducing agent, Int. J. Hydrog. Energy 41 (24) (Jun. 2016) 10103–10119, https://doi.org/10.1016/j.ijhydene.2015.12.129.

[49] K. Piotrowski, K. Mondal, T. Wiltowski, P. Dydo, G. Rizeg, Topochemical approach of kinetics of the reduction of hematite to wüstite, Chem. Eng. J. 131 (1–3) (Jul. 2007) 73–82, https://doi.org/10.1016/j.cej.2006.12.024.

[50] K. Piotrowski, K. Mondal, H. Lorethova, L. Stonawski, T. Szymański, T. Wiltowski, Effect of gas composition on the kinetics of iron oxide reduction in a hydrogen production process, Int. J. Hydrog. Energy 30 (15) (Dec. 2005) 1543–1554, https://doi.org/10.1016/j.ijhydene.2004.10.013.

[51] Y. Hara, S. Kondō, Kinetics of reduction of iron oxide pellets with hydrogen at low temperatures, Trans. Iron Steel Inst. Japan 8 (5) (1968) 300–310, https://doi.org/10.2355/isijinternational1966.8.300.

[52] D. Guo, et al., Kinetics and mechanisms of direct reduction of iron ore-biomass composite pellets with hydrogen gas, Int. J. Hydrog. Energy 40 (14) (Apr. 2015) 4733–4740, https://doi.org/10.1016/j.ijhydene.2015.02.065.

[53] A.Z. Ghadi, M.S. Valipour, M. Biglari, Mathematical modelling of wustite pellet reduction: grain model in comparison with USCM, Ironmak. Steelmak. 43 (6) (Jul. 2016) 418–425, https://doi.org/10.1080/03019233.2015.1135578.

[54] S.M.M. Nouri, H. Ale Ebrahim, E. Jamshidi, Simulation of direct reduction reactor by the grain model, Chem. Eng. J. 166 (2) (Jan. 2011) 704–709, https://doi.org/10.1016/j.cej.2010.11.025.

[55] M. Hosseinzadeh, N. Kasiri, M. Rezaei, Random pore model insights into structural and operational parameters for hydrogen-based iron oxide reduction, Process. Saf. Environ. Prot. 190 (Oct. 2024) 464–480, https://doi.org/10.1016/j.psep.2024.07.054.

[56] J.J. Wong, D. Iruretagoyena, N. Shah, P.S. Fennell, A three-interface random pore model: the reduction of iron oxide in chemical looping and green steel technologies, Proc. R. Soc. A, Proc. Math. Phys. Eng. Sci. 479 (2278) (Oct. 2023), https://doi.org/10.1098/rspa.2023.0173.

[57] Y. Zhai, L. Shao, C. Zhao, X. Zhang, H. Saxén, A numerical study of the thermochemical and aerodynamic states of H_2 -intensive direct reduction shaft furnace, Steel Res. Int. (Nov. 2024), https://doi.org/10.1002/srin.202400567.

[58] F. Mauret, M. Baniasadi, H. Saxén, A. Feiterna, S. Hojda, Impact of hydrogenous gas injection on the blast furnace process: a numerical investigation, Metall. Mater. Trans. B 54 (4) (Aug. 2023) 2137–2158, https://doi.org/10.1007/s11663-023-02822-4.

[59] A. Pineau, N. Kanari, I. Gaballah, Kinetics of reduction of iron oxides by H2. Part I: low temperature reduction of hematite, Thermochim. Acta 447 (1) (Aug. 2006) 89–100, https://doi.org/10.1016/j.tca.2005.10.004.

[60] E. Salucci, A. D'Angelo, V. Russo, H. Grénman, H. Saxén, Review on the reduction kinetics of iron oxides with hydrogen-rich gas: experimental investigation and modeling approaches, Ind. Eng. Chem. Res. 64 (1) (Jan. 2025) 1–35, https://doi.org/10.1021/acs.iecr.4c03136.

[61] A. Loder, S. Santner, M. Siebenhofer, A. Böhm, S. Lux, Reaction kinetics of direct reduction of mineral iron carbonate with hydrogen: determination of the kinetic triplet, Chem. Eng. Res. Des. 188 (Dec. 2022) 575–589, https://doi.org/10.1016/j.cherd.2022.10.007.

[62] S.K. Kuila, R. Chatterjee, D. Ghosh, Kinetics of hydrogen reduction of magnetite ore fines, Int. J. Hydrog. Energy 41 (22) (Jun. 2016) 9256–9266, https://doi.org/10.1016/j.ijhydene.2016.04.075.

[63] H.Y. Lin, Y.W. Chen, C. Li, The mechanism of reduction of iron oxide by hydrogen, Thermochim. Acta 400 (1–2) (Apr. 2003) 61–67, https://doi.org/10.1016/S0040-6031(02)00478-1.
[64] S.S. Miljanic, B.B. Radak, Gas Analysys - an improved mathematical model of thermal conductivity detectors, Bull. Soc. Chim. Beograd 49 (3) (1983) 123–127.
[65] H. Kang, et al., Influence of hydrogen flow rate on multistep kinetics of hematite reduction, Int. J. Hydrog. Energy 49 (Jan. 2024) 1255–1268, https://doi.org/10.1016/j.ijhydene.2023.08.295.
[66] E. Salucci, A. D'Angelo, V. Russo, H. Grénman, H. Saxén, Modelling of iron oxide reduction with hydrogen in a small fixed bed, Chem. Eng. Sci. 292 (Jun. 2024) 119934, https://doi.org/10.1016/j.ces.2024.119934.
[67] M.S. Valipour, Mathematical Modeling of a Non-Catalytic Gas-Solid Reaction: Hematite Pellet Reduction with Syngas, 2009.
[68] Chemstations, CHEMCAD v. 7.0, Accessed: Apr. 23, 2025. [Online]. Available: http://www.chemstations.com/, 2016.
[69] T. Akiyama, H. Ohta, R. Takahashi, Y. Waseda, J. Yagi, Measurement and modeling of thermal conductivity for dense iron oxide and porous Iron ore aggliomerates in stepwise reduction, ISIJ Int. 32 (7) (1992) 829–837, https://doi.org/10.2355/isijinternational.32.829.
[70] O. Hessling, J.B. Fogelström, N. Kojola, D. Sichen, The effect of the endothermic reaction nature on the Iron ore pellet reduction using hydrogen, Metall. Mater. Trans. B Process Metall. Mater. Process. Sci. 53 (2) (Apr. 2022) 1258–1268, https://doi.org/10.1007/s11663-021-02405-1.
[71] O. Hessling, J.B. Fogelström, N. Kojola, J. Martinsson, Influence of water content on the kinetics and mechanisms of hydrogen reduction using industrial iron ore pellets at 873 K–1173 K, ISIJ Int. 64 (10) (Aug. 2024), https://doi.org/10.2355/isijinternational.ISIJINT-2023-443 p. ISIJINT-2023-443.
[72] A. Heidari, T. Ilmakangas, S. Pöyhtäri, E.-P. Heikkinen, P. Sulasalmi, T. Fabritius, The influence of water vapour on hydrogen reduction of iron ore pellets, in: Ironmaking & Steelmaking: Processes, Products and Applications, Jun. 2025, https://doi.org/10.1177/03019233251352979.